Estimating machining forces from vibration measurements

by

Manish Kumar Joddar
Bachelor of Technology (Honors), Indian Institute of Technology (IIT), Kharagpur, 1995
Post Graduate Diploma in Industrial Management, National Institute of Industrial Engineering (NITIE), Mumbai, 1997

A Thesis Submitted in Partial Fulfillment
of the Requirements for the Degree of

MASTER OF APPLIED SCIENCE
in the Department of Mechanical Engineering

University of Victoria

Supervisory Committee

Estimating machining forces from vibration measurements

by

Manish Kumar Joddar
Bachelor of Technology (Honors), Indian Institute of Technology (IIT), Kharagpur, 1995
Post Graduate Diploma in Industrial Management, National Institute of Industrial Engineering (NITIE), Mumbai, 1997

Supervisory Committee

Dr. Keivan Ahmadi, Department of Mechanical Engineering, University of Victoria
Co-Supervisor

Dr. Ben Nadler, Department of Mechanical Engineering, University of Victoria
Co-Supervisor

Dr. Zuomin Dong, Department of Mechanical Engineering, University of Victoria
Departmental Member

Abstract

The topic of force reconstruction has been studied quite extensively but most of the existing research work that has been done are in the domain of structural and civil engineering construction like bridges and beams. Considerable work in force reconstruction has also being done in fabrication of machines and structures like aircrafts, gear boxes etc. The topic of force reconstruction of the cutting forces during a machining process like turning or milling machines is a recent line of research to suffice the requirement of proactive monitoring of forces generated during the operation of the machine tool. The forces causing vibrations while machining if detected and monitored can enhance system productivity and efficiency of the process. The objective of this study was to investigate the algorithms available in literature for inverse force reconstruction and apply for reconstruction of cutting forces while machining on a computer numerically controlled (CNC) machine. This study has applied inverse force reconstruction technique algorithms 1) Deconvolution method, 2) Kalman filter recursive least square and 3) augmented Kalman filter for inverse reconstruction of forces for multi degree of freedom systems.

Results from experiments conducted as part of this thesis work shows the effectiveness of the methods of force reconstruction to monitor the forces generated during the machining process on machine tools in real time without employing dynamometers which are expensive and complex to set-up. This study for developing a cost-effective method of force reconstruction will be instrumental in applications for improving machining efficiency and proactive preventive maintenance.

Table of Contents

List of Tables

List of Figures

Acknowledgments

I want to express gratitude to my advisors, Dr. Keivan Ahmadi, and Dr. Ben Nadler, for the support and mentorship provided to me. I could not have successfully managed to complete this graduate study course in the field of Mechanical Engineering without the able guidance of my advisors. I am grateful to Dr. Ahmadi for the stimulation without which I could not have made it on the steep learning curve required to undertake a pathway towards the MASc course.

I am grateful to Mr. Rodney Katz from Machine Shop, Mr. Patrick Chang from Mechatronics Laboratory, and undergraduate students of the department Raimund Mullin and Patrick Heaney during my set up for the experiments. Their expertise, skills, and experience were of great help in performing the experiments for the thesis.

During my stay in Victoria, I have made fantastic friends. I would like to thank them for the joyful moments and precious memories. I would also like to thank the faculty members, staff, and students of the University of Victoria. I have had an amazing time since September’2017, when I joined this community.

Above all, I would like to thank my beloved family and all my well-wishers. This accomplishment would not be possible without their support and encouragement.

Dedication

To my family

Chapter 1

Introduction

In a machining process, every excitation force applied or generated as part of the process causes a response in the form of vibrations. Vibration during the machining process is a major contributor to error in machining and leads to higher maintenance cost and reduction in productivity of the overall life of the machine. To achieve higher accuracy and productivity, vibration in machining processes must be accurately predicted and controlled. In order to understand the forces generating vibrations during a machining process it is required to have force sensors installed on the machine to measure such forces generated during machining. Normally, forces generated during a machining process are measured by dynamometers fixed on the machine tool [Najeh Tounsi, 2000]. Furthermore, the vibration response due to excitation forces can be measured by strain gauges or accelerometers [J.Knapp, 1998]. Although dynamometers are easily available and widely used in the industry, they are cumbersome [R.Transchel, 2012] and not economical [Yafei Qin, 2017].

Effects of vibration during machining, its impact on both post processing and real-time monitoring of the forces causing vibrations is an area that is being widely researched. Therefore, this study attempted to examine various algorithm based techniques to monitor the excitation forces in real time and investigate alternate methods for force measurement compared with conventional tools like dynamometers.

1.1 Thesis Motivation

Although forces can be monitored by use of table dynamometers [Wan, Yin, Zhang, 2016], which can be installed on the table of the machine tool, this installation is not cost-effective and these devices acquire a lot of space on the table of the machine tool, limits geometry and dimensions of the work piece, complicated installation requiring clamping between work piece and table of machine tool, thus compromising machine performance and productivity [Yafei Qin, 2017]. To solve this quandary, this study employed the use of accelerometers that are relatively inexpensive to procure, maintain and install on the machine to measure the vibration responses. Next, the prospect of using mathematical algorithms to inverse calculate the forces from the vibration responses was explored using algorithms 1) Deconvolution Method, 2) Kalman Filter & Recursive Least Square and 3) Augmented Kalman Filter.

1.2 Thesis Outline

The thesis has been structured into five chapters dealing with the various aspects of the thesis, as listed below:

Chapter 1 An introduction to the objective and motivation to this study dealing with force reconstruction methods which can be applied towards estimation of cutting forces on a machine tool

Chapter 2 A literature review of available force reconstruction techniques and existing work on the application of inverse force reconstruction techniques. The techniques reviewed in this chapter are

1. Deconvolution Method
2. Kalman Filter Recursive Least Square
3. Augmented Kalman Filter

Chapter 3 Simulation of algorithms for inverse reconstruction of forces using Matlab. Details on experimental verification of effectiveness of inverse reconstruction of forces.

Chapter 4 Details of experiments conducted on Computer Numerically Controlled (CNC) machine for verification of inverse force reconstruction of cutting forces

Chapter 5 Conclusion and Future work

Chapter 2

Background and Literature Review

This chapter provides details, from literature review, on inverse reconstruction of force from measured vibration responses. In addition, focus has been laid on the algorithms used for the force reconstruction that will be applied later on the experiments. Covered here are the core aspects of the inverse force reconstruction techniques of deconvolution method, Kalman filter recursive least square, augmented Kalman filter and regularization factor for handling ill-conditioned matrices for inverse force reconstruction.

2.1 Inverse and Forward Problem

In the field of vibration analysis, the behavior of the system is studied using a mathematical model depicting the system. Forward problem is one where the forces are known but the system response is unknown. In such cases where the input forces are known and the goal is to understand the system response is termed as forward problem.

Likewise, in an opposite scenario where the input forces are not known or may not be possible to measure but the system response is known, we measure the response of the system. Interestingly, the input forces acting on the systems, which can also be considered as the excitation forces can be calculated from the system response. This is the reverse of forward problem and is termed as inverse problem.

Some methods available in the literature and discussed in this chapter for solving the inverse problem have been adopted in this study. In case of the inverse problem, the challenges of getting consistent solution are enhanced by inherent noise present in the system. Ill conditioning and non-uniqueness of solution, requiring much more analysis and rigor for getting a solution when compared to forward problem, affects the inverse problem’s solution.

The focus of this thesis is on three methodologies for solution to inverse problem, for reconstructing the excitation forces generated during machining processes. The methodologies are:

1) Regularization of deconvolution problem
2) Kalman filter and recursive least square

3) Augmented Kalman filter

2.2 Regularization of deconvolution problem

In this method, dynamic or excitation forces are recovered using inverse problem by deconvolution of the force signals from the measured system responses. Researches in deconvolution problem have been using both the frequency and time domain methods. Researchers like J.F. Doyle [Doyle, 1984] have explored the frequency domain method whereas others including [C. Chang, 1989], [E, A, P, 2003] have done it in the time domain method.

Time domain deconvolution method has been used for force reconstruction in this work.

2.2.1 Time domain deconvolution

The method of time domain deconvolution to reconstruct the forces by means of indirect measurements consists of recording the response at location, a, and at time t. The response can be measured as strain, displacement, velocity or acceleration. Although vibration responses in any of the forms as strain, displacement, velocity and acceleration can be used for time domain deconvolution, in this chapter displacement, x (b, a, t), is being considered to suffice for the explanation of the concept of deconvolution method. Displacement, x (b, a, t), measured at location, a, and at time, t, due to an excitation force f(b,t), at location b and at time t is represented as

$$\mathrm{x}\ (\mathrm{b}, \mathrm{a}, \mathrm{t}) = \int_0^t g(b,a,t-\tau)f(b,\tau)d\tau = g(b,a,t) * f(b,t). \qquad (1)$$

In the integral equation (1), $g(b,a,t)$ is the impulse response function between the points b and a. The functions $g(b,a,t)$ and $f\,(b,t)$ have a convolution operator, $*$ between them representing a convolution of $g(b,a,t)$ and $f(b,t)$.

Time sampling of the convolution equation leads to discretization in time domain and the solution is represented as

$$[X] = [G][F], \qquad (2)$$

$$[X] = [x(b,a,\Delta t), x(b,a,2\Delta t), \dots\dots, x(b,a,n\Delta t)]^T, \qquad (3)$$

$$[F] = [f(b,0), f(b,\Delta t), \dots\dots, f(b,(n-1)\Delta t)]^T. \qquad (4)$$

$[X] \in \mathbb{R}^{n}$ and $[F] \in \mathbb{R}^{n}$ are the vibration response vector and the force vector, the superscript ‘T’ denotes transpose of a vector or a matrix and Δt is the sampling time. The transfer function, $[G] \in \mathbb{R}^{nxn}$ in matrix form is represented as

$$[G] = \Delta t \begin{bmatrix} g(b,a,\Delta t) & 0 & \ldots\ldots\ldots\ldots\ldots & 0 \\ g(b,a,2\Delta t) & g(b,a,\Delta t) & \ldots\ldots\ldots\ldots & 0 \\ g(b,a,3\Delta t) & g(b,a,2\Delta t) & \ldots\ldots\ldots & 0 \\ \ldots\ldots & \ldots\ldots\ldots\ldots & \ldots\ldots\ldots\ldots & 0 \\ \ldots\ldots & \ldots\ldots\ldots\ldots & \ldots\ldots\ldots\ldots & 0 \\ g(b,a,n\Delta t) & g(b,a,(n-1)\Delta t) & \ldots\ldots\ldots\ldots & g(b,a,\Delta t) \end{bmatrix}. \tag{5}$$

Some researchers [Yen, Shin, Enboa, 1995] have termed the matrix $[G]$ as Green’s function matrix. Excitation forces are obtained by deconvolution of the equation (1) as

$$[F] = [G]^{-1}[X]. \tag{6}$$

The deconvolution problem depends on the condition number of the matrix $[G]$ and can be ill-posed [Yen, Shin, Enboa, 1995]resulting in large deviations in the outcome, leading to erroneous results. The ill-posed problem is due to ill-conditioning of the matrix $[G]$ and thus equation (2) is numerically insolvable and in cases of an existence of solution, due to ill-conditioning large deviations occur in the results even for a small noise disturbances in the system.

The matrix $[G]$ is decomposed using Singular Value Decomposition (SVD) as

$$[G] = [U][\sum][V]^{T} = \sum_{i=1}^{n} [u]_{i}\, \sigma_{i} [v]_{i}^{T}. \tag{7}$$

Considering the matrix $[G] \in \mathbb{R}^{mxn}$ ($m \geq n$) is a real matrix. Here, $[u]_{i} \in \mathbb{R}^{m}$ are the left singular vectors of the matrix $[U] \in \mathbb{R}^{mxm}$, $[v]_{i} \in \mathbb{R}^{n}$ are the right singular vectors of the matrix $[V] \in \mathbb{R}^{nxn}$ and $[u]_{1} \ldots [u]_{m}$ form the orthonormal basis for the range of the matrix $[G]$ and $[v]_{1} \ldots [v]_{n}$ form the orthonormal basis for the range $[G]^{T}$. The matrices $[U]$ and $[V]$ are the left and right singular matrix. The matrix, $[\sum] \in \mathbb{R}^{mxn}$ is a diagonal matrix that consists of the singular values, σ_{i} ($i = 1 \ldots n$), of $[G]$ as its diagonal elements.

Inverse method for calculation of force using the decomposed components of the matrix$[G]$, gives the n-component force vector $[F] \in \mathbb{R}^{n}$ as

$$[F] = \sum_{i=1}^{n} \frac{[u]_{i}^{T}[X]\,[v]_{i}}{\sigma_{i}}. \tag{8}$$

The solution to the above deconvolution problem for reconstructing the force largely depends on the singular values and singular vectors of the matrix $[G]$. Therefore, the solution can be ill-posed in case of ill-conditioning (i.e. near zero singular values) and rank deficient.

Ill-conditioning and sensitivity of the solution to noise is solved by regularization. Regularization results in the modification of the initial problem and leads to a robust solution. Although, there are various regularization techniques available in literature, this research has focused on the use of Tikhonov's technique to estimate a regularization factor to be used for estimating the forces by the deconvolution [E. Jacquelin, 2003] method.

2.2.2 Tikhonov Regularization

The Tikhonov's [M. E. HOCHSTENBACH, December 9, 2013] regularization method consists of finding a trade-off between the residual or error norm of equation (2) and the smoothing norm defined as $\varphi([F])$. The problem is then regularized as

$$\min_{F}\{\| [G][F] - [X]\|_2\} \text{ subject to } \min_{F}\{\varphi([F])\}. \tag{9}$$

The error norm is $\| [G][F] - [S]\|_2$ and the smoothing norm takes the form

$$\varphi([F]) = \| [L][F]\|_2. \tag{10}$$

Here, $[L]$ is often the identity, (E, A, & P, 2003), operator (I).

The problem in equation (9) is equivalent, (E, A, & P, 2003), to

$$\min_{F}\{\| [G][F] - [X]\|_2 + \alpha\, \varphi([F])\ \} \text{ and } \varphi([F]) =\| [L][F]\|_2. \tag{11}$$

Here, α is termed as regularization parameter. The choice of α is a trade-off and allows to single out a minimum of the residual norm of equation (2) or a minimum of the smoothing norm.

In solving the regularization problem, the regularization quality is dependent on the regularization parameter used so the methodology for choosing the right value is of utmost importance. In the thesis, the method of L-curve [E. Jacquelin, 2003] was used for choosing the value of the regularization parameter. In order to obtain the L-curve, it is required to plot the log-log curve of the smoothing norm versus the residual norm mentioned on equations (9)-(11). The L-curve, [Hochstenbach, Reichel, Rodriguez, 2013], [Hansen, Christian, O' Leary, Prost, 1993], gives an approximation technique for the choice of value for regularization parameter. The curve takes the shape of 'L' with the horizontal and vertical branches merging at the "corner" taking the shape of the letter L. The value of, α at the "corner" of the curve gives the best compromise fitment for the data to sufficiently regularize the solution.

2.3 Online linear regression estimator - Kalman filter recursive least square

The Kalman filter recursive least square method is an online (recursive) estimator. Literature reviewed e.g.; [C.-K. Ma, 2003], [Jui-Jung Liu, 2000] and [Pan-Chio Tuan, 19 Apr 2007] have discussed on this online estimation technique for the reconstruction of force. Kalman Filter [KALMAN, 1960] is used widely in various fields in applied science and engineering namely inertial navigation, sensor calibration, radar tracking, manufacturing, economics, signal processing, freeway traffic modeling, etc. and is considered to provide optimal solutions for tracking and prediction. The thesis studies this technique of online estimation of the excitation forces from the vibration responses using this method. This method has 2(two) parts, the Kalman filtering and the other being the recursive least square. Recursive least square part is dependent on inputs from the Kalman filter part.

2.3.1 Kalman filter

Prediction and correction are the two (2) parts of the Kalman filter algorithm. This subsection describes the concept of this algorithm using an n-degree of freedom system. Continuous time state space model is converted to discrete time state space model, subsequently observed measurements of the states are used to estimate the input and output states.

2.3.1.1 State Space in continuous and discrete time

The differential equation of motion of a Multi-Degree of Freedom (MDOF) linear vibratory system [Paul Zarchan, September 2000] in terms of mass, stiffness and damping matrices of the system (Meirovitch, 1986) is represented as

$$[\mathrm{M}][\ddot{\mathrm{Y}}(\mathrm{t})] + [\mathrm{C}]\,[\dot{\mathrm{Y}}(\mathrm{t})] + [\mathrm{K}][\mathrm{Y}(\mathrm{t})] = [\mathrm{F}(\mathrm{t})]. \tag{12}$$

Continuous time state space representation of equation (12) is

$$\left[\dot{X}(t)\right] = [A]\,[X(t)] + [B]\,[F(t)], \tag{13}$$

$$[Z(t)] = [H]\,[X(t)]\,. \tag{14}$$

Here, the matrices and vectors on the equations (13) - (14) are as

$$[A] = \begin{bmatrix} 0_{nxn} & I_{nxn} \\ -M^{-1}K & -M^{-1}C \end{bmatrix}, \; [B] = \begin{bmatrix} 0_{nxn} \\ M^{-1} \end{bmatrix},$$

$$[X(t)] = \left[Y_1(t)\ \dot{Y}_1(t) \ldots\ldots\ldots Y_n(t)\ \dot{Y}_n(t)\right]^T \tag{15}$$

or

$$[X(t)] = [X_1(t)\ X_2(t) \ldots.\ X_{2n-1}(t)\ X_{2n}(t)]^T$$

and

$$[F(t)] = [F_1(t)\ F_2(t) \ldots\ldots\ldots F_n(t)]^T. \tag{16}$$

Here, $[M] \in \mathbb{R}^{nxn}$, $[C] \in \mathbb{R}^{nxn}$ and $[K] \in \mathbb{R}^{nxn}$ denotes the mass, damping and stiffness matrices respectively. $[F(t)] \in \mathbb{R}^{n}$ is an input force vector. $[\ddot{Y}(t)] \in \mathbb{R}^{n}$, $[\dot{Y}(t)] \in \mathbb{R}^{n}$ and $[Y(t)] \in \mathbb{R}^{n}$ denotes the acceleration, velocity and displacement vectors respectively. $[X(t)] \in \mathbb{R}^{2n}$ denotes the states vector of the system. $[Z(t)] \in \mathbb{R}^{2n}$ is the observation vector.

The measurement matrix, $[H] \in \mathbb{R}^{2nx2n}$ of the states being I_{2nx2n}. The equations, (13) and (14), when converted to discrete time with an intervals of Δt, and associated with a process and measurement noise, are represented as

$$[X(k+1)] = [\emptyset][X(k)] + [\Gamma][[F(k)] + [w(k)]]\,, \tag{17}$$

$$[Z(k)] = [H][X(k)] + [v(k)]. \tag{18}$$

Here, $[X(k)] \in \mathbb{R}^{2n}$ is the state vector at the discrete time step of k, $[\emptyset] \in \mathbb{R}^{2nx2n}$ is the state transition matrix, $[\Gamma] \in \mathbb{R}^{2nxn}$ is the input matrix, $[F(k)] \in \mathbb{R}^{n}$ is the deterministic input vector, $[w(k)] \in \mathbb{R}^{n}$ is the additive noise vector and $[v(k)] \in \mathbb{R}^{n}$ is the measurement noise vector. $[\emptyset]$ and $[\Gamma]$ are obtained from the system matrices [A] and [B] as

$$[\emptyset] = \exp([A]\ \Delta t), \tag{19}$$

$$[\Gamma] = \int_{k\Delta t}^{(k+1)\Delta t} \exp\{[A][(k+1)\Delta t - \tau]\}\,[B]d\tau. \tag{20}$$

The noise vectors are assumed Gaussian with zero mean white noise [Paul Zarchan, September 2000]. The respective co-variances, $[Q] \in \mathbb{R}^{2nx2n}$ and $[R] \in \mathbb{R}^{2nx2n}$, of process and measurement noise at times i and j are as

$$E[[w]_i, [w]_j^T] = [Q]\delta_{ij}, \tag{21}$$

$$[Q] = Q_w \, I_{2nx2n} \text{ and } Q_w = \sigma_w^2,$$

$$E[[v]_i, [v]_j^T] = [R]\delta_{ij}, \tag{22}$$

$$[R] = R_v \, I_{2nx2n} \text{ and } R_v = \sigma_v^2.$$

The standard deviation of respective noises are σ_w and σ_v. E is the expected value operator. The Kalman filter equations starts with calculating the state estimates

$$[\overline{X}(k \mid k-1)] = [\emptyset][\overline{X}(k-1 \mid k-1)]. \tag{23}$$

Here, $[\overline{X}(k \mid k-1)] \in \mathbb{R}^{2n}$ represents the state estimate for the discrete time step, k, based on the estimate of the previous, $[\overline{X}(k-1 \mid k-1)] \in \mathbb{R}^{2n}$ estimation step. The updated estimate for the discrete time step, k, of the iteration is calculated as

$$[\overline{X}(k \mid k)] = [\overline{X}(k \mid k-1)] + K_a(k)[\overline{Z}(k)]. \tag{24}$$

Here, $[\overline{Z}(k)] \in \mathbb{R}^{2n}$ is the innovation and is calculated as

$$[\overline{Z}(k)] = [Z(k)] - [H][\overline{X}(k \mid k-1)]. \tag{25}$$

Here, $[K_a(k)] \in \mathbb{R}^{2nx2n}$ is the Kalman gain of the filter and is calculated as

$$[K_a(k)] = [P(k \mid k-1)][H]^T[S(k)]^{-1}. \tag{26}$$

Here, $[P(k \mid k-1)] \in \mathbb{R}^{2n}$ is the filter's error covariance matrix and is calculated as

$$[P(k \mid k-1)] = [\emptyset][P(k-1 \mid k-1)][\emptyset]^T + [\Gamma][Q][\Gamma]^T. \tag{27}$$

Here, $[S(k)] \in \mathbb{R}^{2nx2n}$ is the innovation covariance and is calculated as

$$[S(k)] = [H][P(k \mid k-1)][H]^T + [R]. \tag{28}$$

The updated estimates for the next step of the iteration for the error covariance is calculated as

$$[P(k \mid k)] = [I - K_a(k)[H]]\,[P(k \mid k-1)]. \tag{29}$$

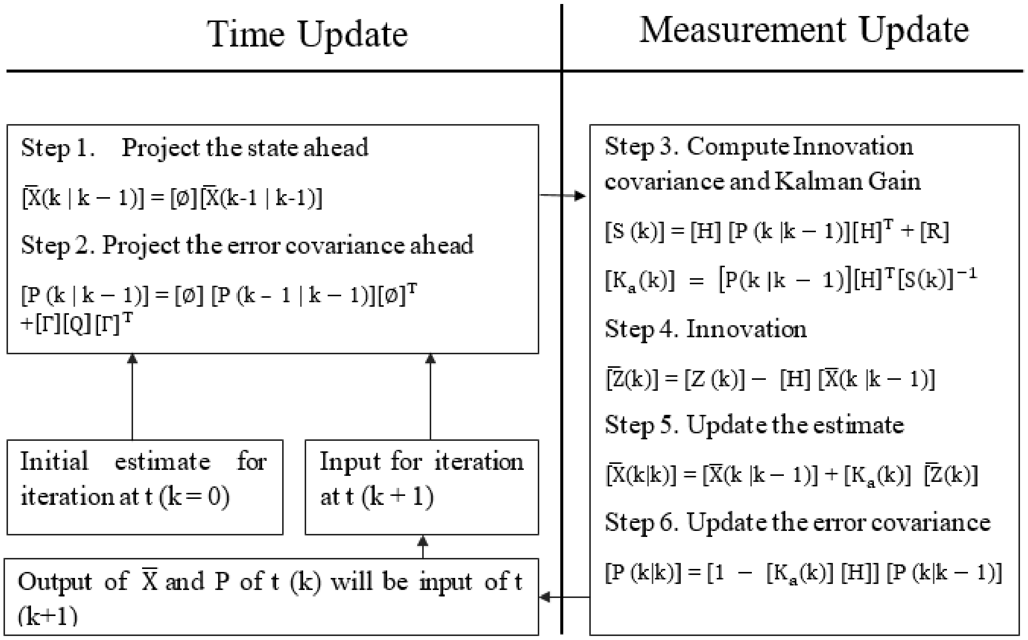

Figure 1. Flow chart for the steps of time and measurement updates of Kalman filter.

2.3.2 Recursive Least Square (RLS)

The RLS estimator algorithm provided in literature [C.-K. Ma, 2003] [Jui-Jung Liu, 2000], was initially used for estimation of heat flux [Pan-Chio Tuan, 19 Apr 2007]. RLS starts by computing the sensitivity matrices as

$$[B_s(k)] = [H]\,[[\emptyset][M_s(k-1)] + I][\,\Gamma], \tag{30}$$

$$[M_s(k)] = [I - [K_a(k)][H]]\,[[\,\emptyset]\,[M_s(k-1)] + I]. \tag{31}$$

Here, $[B_s(k)] \in \mathbb{R}^{2nx2n}$ and $[M_s(k)] \in \mathbb{R}^{2nx2n}$ are the sensitivity matrices. Next, $[K_b(k)] \in \mathbb{R}^{2nx2n}$, the correction gain, is calculated as

$$[K_b(k)] = \gamma^{-1}[P_b(k-1)]\,[B_s(k)]^T[[B_s(k)]\,\gamma^{-1}[P_b(k-1)][B_s(k)]^T + [S(k)]]^{-1}. \tag{32}$$

The scalar parameter, γ is the fading factor and ranges between $0 < \gamma \leq 1$,

$$[P_b(k)] = [1 - [K_b(k)][B_s(k)]]\,\gamma^{-1}[P_b(k-1)]. \tag{33}$$

The fading factor is the compromise between the fast adaptability and loss of estimation accuracy. The matrix $[P_b(k)] \in \mathbb{R}^{2nx2n}$ is the error covariance of the estimated input vector. Initial value of the sensitivity matrix $[M_s(k)]$ is usually taken as zero to start with and the matrix $[B_s(k)]$ is computed accordingly by equation (30). The fading factor $0 < \gamma < 1$, helps in not letting $[K_b(k)]$ get to zero and allows the algorithm to continuously update the estimate of the force for each iteration cycle, and $\gamma = 1$, the algorithm reduces to that of the usual sequential least squares, which is suitable only for a constant-parameter system. The force estimate for each discrete step is computed as

$$[\hat{F}(k)] = [\hat{F}(k-1)] + [K_b(k)][\,[\bar{Z}(k)] - [B_s(k)][\hat{F}(k-1)]] \,. \tag{34}$$

The values taken from the Kalman filter in each iteration cycle are$[K_a(k)]$, $[S(k)]$ and $[\bar{Z}(k)] \in \mathbb{R}^{2n}$ respectively. $[\hat{F}(k)] \in \mathbb{R}^{n}$, is the estimate of the input vector.

The detailed derivation on Kalman filter and RLS algorithm, significance of fading factor γ and the correction gain $[K_b(k)]$, are out of the scope for this thesis. Interested readers are referred to [Pan-Chio Tuan, 19 Apr 2007].

Figure 2, illustrates the dependency of RLS on the Kalman filter algorithm, initiation of values in RLS and input parameters from Kalman filter to RLS. The algorithms are interdependent and these estimate the forces from the measured values of the system response at each regression step.

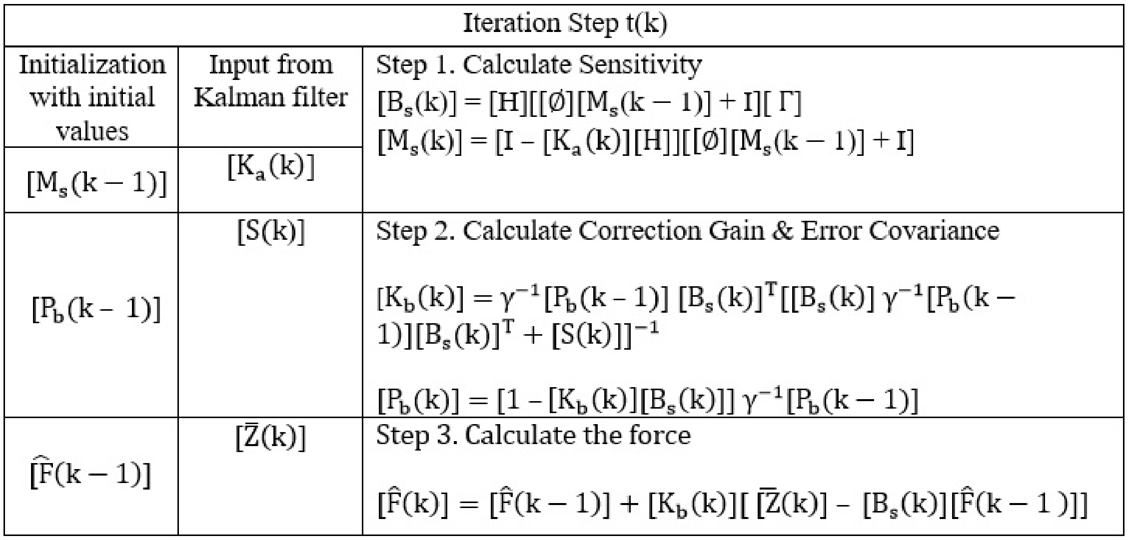

Iteration Step t(k)		
Initialization with initial values	Input from Kalman filter	Step 1. Calculate Sensitivity $[B_s(k)] = [H][[\emptyset][M_s(k-1)] + I][\Gamma]$ $[M_s(k)] = [I - [K_a(k)][H]][[\emptyset][M_s(k-1)] + I]$
$[M_s(k-1)]$	$[K_a(k)]$	
$[P_b(k-1)]$	$[S(k)]$	Step 2. Calculate Correction Gain & Error Covariance $[K_b(k)] = \gamma^{-1}[P_b(k-1)]\,[B_s(k)]^T[[B_s(k)]\,\gamma^{-1}[P_b(k-1)][B_s(k)]^T + [S(k)]]^{-1}$ $[P_b(k)] = [1 - [K_b(k)][B_s(k)]]\,\gamma^{-1}[P_b(k-1)]$
$[\hat{F}(k-1)]$	$[\bar{Z}(k)]$	Step 3. Calculate the force $[\hat{F}(k)] = [\hat{F}(k-1)] + [K_b(k)][\,[\bar{Z}(k)] - [B_s(k)][\hat{F}(k-1)]]$

Figure 2. Initialization and inputs from Kalman filter to the important steps of RLS

2.3.3 Augmented Kalman filter

The augmented Kalman filter [E. Lourens, 2012] method, also an inverse online force reconstruction method, is a deterministic-stochastic method for the reconstruction of excitation forces. In case of augmented Kalman filter the state-space vector is augmented to include the input, excitation force, state.

2.3.3.1 Augmented state space model

Similar to the Kalman filter recursive least square method the augmented Kalman filter method starts with a continuous time state space model. But in case of the augmented Kalman filter method, the discrete time state space equations are augmented to achieve the augmented state equation.

The discrete time state space equation [E. Lourens, 2012] for the states, $[X(k)] \in \mathbb{R}^{2n}$ and the input forces $[F(k)] \in \mathbb{R}^{n}$ is

$$[X\,(k+1)] = [\emptyset][X(k)] + [\Gamma][F(k)] + [w(k)]. \tag{35}$$

Here, $[w(k)] \in \mathbb{R}^{n}$ denotes the noise vector of the process. The input force vector is assumed to be a constant with the stochastic component, $[\eta(k)] \in \mathbb{R}^{n}$ as

$$[F(k+1)] = [F(k)] + [\eta(k)]. \tag{36}$$

Here, $[\eta(k)]$ denotes a force increment, stochastic, component of the process. The force time history is generated with an appropriate choice of the covariance matrix for the component $[\eta(k)]$.

The input, $[F(k)]$, gets added into the state vector to form the augmented state vector, $[X^a(k)]$ and is represented as

$$[X^a(k+1)] = [A_a][X^a(k)] + [\xi(k)]. \tag{37}$$

The values $[X^a(k)] \in \mathbb{R}^{3n}$ and $[\xi(k)] \in \mathbb{R}^{3n}$ are

$$[X^a(k)] = \begin{bmatrix}[X(k)]\\ [F(k)]\end{bmatrix}, \ [\xi(k)] = \begin{bmatrix}[w(k)]\\ [\eta(k)]\end{bmatrix}. \tag{38}$$

Subsequently, the measurements are also expressed in terms of the augmented state as

$$[d_k] = [G_a][X^a(k)] + [v(k)]. \tag{39}$$

Here, the matrices $[A_a] \in \mathbb{R}^{3nx3n}$ and $[G_a] \in \mathbb{R}^{3nx3n}$ are the augmented state and augmented measurement matrices respectively of the augmented state space model.

Here, $[d_k] \in \mathbb{R}^{3n}$ is the measured data vector and $[v(k)] \in \mathbb{R}^{3n}$ is the measurement noise vector. The direct transmission matrix, $[J] \in \mathbb{R}^{3nxn}$ is placed with output influence matrix,

$[G] \in \mathbb{R}^{3nx2n}$, to form the $[G_a]$ matrix (E, Reynders, DeRoeck, Degrande, & G.Lombaert, 2012) as

$$[A_a] = \begin{bmatrix} [\emptyset] & [\Gamma] \\ 0_{nx2n} & I_{nxn} \end{bmatrix}, [G_a] = [[G] \quad [J]]. \tag{40}$$

The stochastic processes $[w(k)]$ and $[\eta(k)]$, and the measurement, $[v(k)]$ noises are assumed to be stationary, mutually uncorrelated with zero mean. The respective co-variance, $[Q] \in \mathbb{R}^{2nx2n}$ $[R] \in \mathbb{R}^{3nx3n}$ and $[S] \in \mathbb{R}^{nxn}$, at times i and j are as

$$E[[w]_i, [w]_j^T] = [Q]\delta_{ij}. \tag{41}$$

Here, $[Q] = Q_w I_{2nx2n}$, with distribution standard deviation of $Q_w = \sigma_w$.

$$E[[v]_i, [v]_j^T] = [R]\delta_{ij}. \tag{42}$$

Here, $[R] = R_v\, I_{3nx3n}$, with distribution standard deviation of $R_v = \sigma_v$.

$$E[[\eta]_i, [\eta]_j^T] = [S]\delta_{ij}. \tag{43}$$

Here, $[S] = S_\eta I_{nxn}$ with distribution standard deviation of $S_\eta = \sigma_\eta$ respectively. E is the expected value operator.

The measurement and time update steps for estimation of the forces after the creation of the augmented states are similar to the Kalman filter algorithm. The augmented Kalman filter equations starts with calculating the state estimates

$$[\overline{X}^a(k \mid k-1)] = [A_a][\overline{X}^a(k-1 \mid k-1)]. \tag{44}$$

Here, $[\overline{X}^a(k \mid k-1)] \in \mathbb{R}^{3n}$ represents the state estimate for k based on the previous states estimate. The updated estimates for the next step of the states for the iteration is computed as

$$[\overline{X}^a(k \mid k)] = [\overline{X}^a(k \mid k-1)] + [L_k][[d_k] - [G_a][\overline{X}^a(k \mid k-1)]]. \tag{45}$$

Here $[d_k]$, represents the measurements of the vibration responses in the states.

The innovation here in equation (45) of the augmented Kalman filter is $[[d_k] - [G_a][\overline{X}^a(k \mid k-1)]]$. $[L_k] \in \mathbb{R}^{3nx3n}$ is the gain of the augmented Kalman filter and is computed as

$$[L_k] = [P(k \mid k-1)][[G_a]^T][SS(k)]^{-1}. \tag{46}$$

Here, $[SS(k)] \in \mathbb{R}^{3nx3n}$ is the innovation covariance and is calculated as

$$[SS(k)] = [G_a][P(k \mid k-1)][G_a]^T + [R]. \tag{47}$$

Here, $[P(k \mid k-1)] \in \mathbb{R}^{3nx3n}$ is the filter's error covariance matrix and is calculated as

$$[P(k\,|\,k-1)] = [A_a][P(k-1\,|\,k-1)][A_a]^T + [Q_a]. \tag{48}$$

Here, $[Q_a] \in \mathbb{R}^{3nx3n}$ is the augmented covariance matrix and is represented as

$$[Q_a] = \begin{bmatrix} [Q] & 0_{2nxn} \\ 0_{nx2n} & [S] \end{bmatrix}. \tag{49}$$

The diagonal values of the matrix $[S]$, in the augmented covariance matrix $[Q_a]$, is calculated using the L-curve [E, Reynders, DeRoeck, Degrande, G.Lombaert, 2012].

The updated estimates for the error covariance for the next step of the iteration is computed as

$$[P(k\,|\,k)] = [I_{3nx3n} - [L_k][G_a]]\,[P(k\,|\,k-1)]. \tag{50}$$

Figure 3 shows the flow chart of the steps for augmented Kalman filter algorithm.

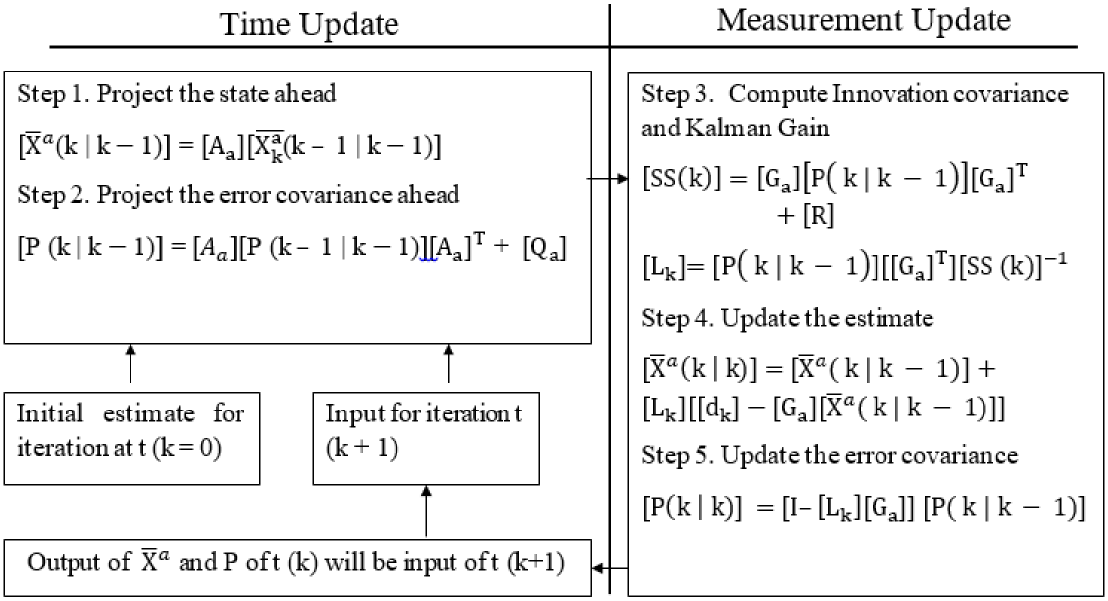

Figure 3. Flow chart of important steps of augmented Kalman filter algorithm

The co-variance $[S]$, is considered the regularization matrix and is used for regulating the smoothing norm of the L-curve. The smoothing norm can be represented as $\sum_{k=1}^{N}\{\|[\overline{F}(k)]\|_2^2\}$ while the error norm depends on the forces along with the state estimates and is represented as $\sum_{k=1}^{N}\{\|[d_k] - ([G][\overline{X}(k)] - [J][\overline{F}(k)])\|_2^2\}$. The L-curve method used in augmented Kalman filter to compute the optimal values of [S], does not exhibit the classical L-shape, and it has been found that for an optimal range of the values of [S], the smoothing norm is insensitive to change in , [S], and error norm where an optimal [S], exists.

Chapter 3

Algorithm Simulation and Verification

This chapter presents a numerical and an experimental example to study the performance of the three force reconstruction algorithms: deconvolution method, Kalman filter recursive least square (RLS) and augmented Kalman filter. In both the numerical and experimental case studies, a known sinusoidal force was applied to the system, and then it was reconstructed from the vibration response.

The presented numerical and experimental case studies serve to explain the implementation of the three (3) force reconstruction algorithms; they also provide insight into the suitability, of the algorithms, for machining applications.

3.1 Numerical case study

The numerical simulation for the study of force reconstruction using the algorithms was conducted on a three (3) degree of freedom system model. The model was chosen with defined mass, stiffness and damping matrices. Figure 4, shows the model that was considered for numerical simulation.

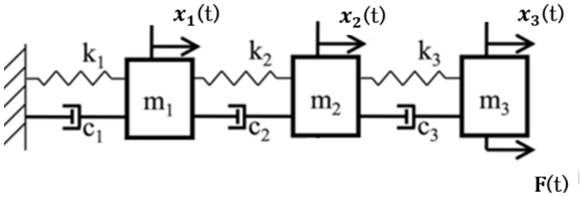

Figure 4. Mass-Stiffness-Damping three (3) DOF model

The model, as depicted on Figure 4 has a sinusoidal excitation force, F(t), applied at m_3. The responses to the excitation forces are $\mathrm{x}_1(\mathrm{t})$, $\mathrm{x}_2(\mathrm{t})$ and $\mathrm{x}_3(\mathrm{t})$ at the locations of the lumped masses m_1, m_2 and m_3 respectively. The corresponding damping and stiffness on the model are represented as c_1, c_2 and c_3, and k_1, k_2 and k_3 respectively. Table 1, shows the mass, stiffness and damping values applied on the simulation.

m_1	10kg	k_1	80000 N/m	c_1	100 N-sec/m
m_2	10kg	k_2	80000 N/m	c_2	100 N-sec/m
m_3	10kg	k_3	80000 N/m	c_3	100 N-sec/m

Table 1. Values of mass, stiffness and damping for a 3-DOF Mass-Stiffness-Damping model

The natural frequency of this system on Table 1 are ω_1 = 6.33 Hz, ω_2 = 17.75 Hz and ω_3 = 25.65Hz respectively. First, this model is tested for a low frequency sinusoidal excitation force of magnitude F_0=1N and frequency f = 2Hz as

$$\mathrm{F(t) = F_o sin2\pi ft.} \tag{51}$$

The excitation force applied for the simulation is on Figure 5.

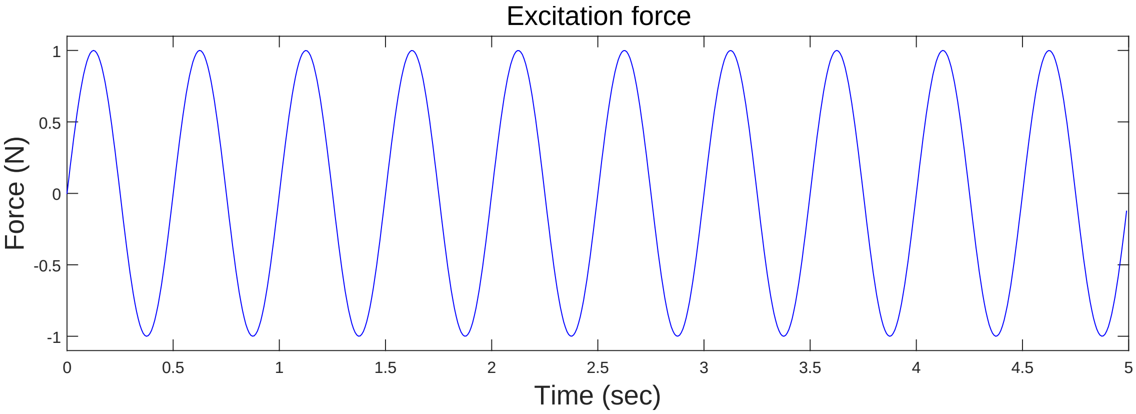

Figure 5. Sinusoidal excitation force of amplitude of 1N and frequency of 2Hz

The first step on the respective simulations was of creating the state-space model with the mass-damping-stiffness matrices. Refer to equations (12) - (16) from Chapter 2.

In the state space equation, the corresponding state, input, output and feedthrough matrices are

$$[\mathrm{A}] = \begin{bmatrix} 0_{3x3} & \mathrm{I}_{3x3} \\ -[\mathrm{M}]^{-1}[\mathrm{K}] & -[\mathrm{M}]^{-1}[\mathrm{C}] \end{bmatrix}, [\mathrm{B}] = \begin{bmatrix} 0_{3x3} \\ [\mathrm{M}]^{-1} \end{bmatrix}, [\mathrm{C}] = [\mathrm{I}_{3x3}, 0_{3x3}] \text{ and } \mathrm{D} = 0. \tag{52}$$

The mass $[\mathrm{M}] \in \mathbb{R}^{3x3}$, stiffness $[\mathrm{K}] \in \mathbb{R}^{3x3}$, and damping $[\mathrm{C}] \in \mathbb{R}^{3x3}$ matrices of the 3DOF system shown on Figure 4 are constructed using the values given in Table 1 as

$$[\mathrm{M}] = \begin{bmatrix} m_1 & 0 & 0 \\ 0 & m_2 & 0 \\ 0 & 0 & m_3 \end{bmatrix}, \tag{53}$$

$$[\mathrm{K}] = \begin{bmatrix} k_1 + k_2 & -k_2 & 0 \\ -k_2 & k_2 + k_3 & -k_3 \\ 0 & -k_3 & k_3 \end{bmatrix}, \tag{54}$$

$$[\mathrm{C}] = \begin{bmatrix} c_1 + c_2 & -c_2 & 0 \\ -c_2 & c_2 + c_3 & -c_3 \\ 0 & -c_3 & c_3 \end{bmatrix}. \tag{55}$$

The next step on the simulations was to convert the continuous time state space model to discrete time state space model for the methods of Kalman filter recursive least square and augmented Kalman filter as shown in equations (17)-(18) and (35)-(36) respectively from Chapter 2. The continuous to discrete time state space conversion was done with zero order hold (ZOH) sampling.

3.1.1 Reconstruction using Deconvolution method

Implementation of the deconvolution method lays on the foundation of generating the Greens function matrix from the impulse responses as shown in equation (5), from Chapter 2. These matrices are generated for the 3 (three) locations corresponding to the 3 (three) degrees of freedom. The individual Greens function matrices generated are referred to as [G1], [G2] and [G3] respectively.

The construction of these matrices was done by calculating the impulse responses at m_1, m_2 and m_3 due to a unit impulse applied at location m_3. Considering the impulse responses at m_1 to be represented as g(3,1, Δt), g(3,1, 2Δt), g(3,1, 3Δt) to g(3,1, nΔt), at m_2 represented as g(3,2, Δt), g(3,2, 2Δt), g(3,2, 3Δt) to g(3,2, nΔt), and similarly at m_3 are represented as g(3,3, Δt), g(3,3, 2Δt), g(3,3, 3Δt) to g(3,3, nΔt). The total duration the force was applied on the model is represented as nΔt. The values of the impulse responses at m_1, m_2 and m_3 are organized, as shown in equation (5) of Chapter 2, into the respective Greens functions matrices of $[G1] \in \mathbb{R}^{nxn}$, $[G2] \in \mathbb{R}^{nxn}$ and $[G3] \in \mathbb{R}^{nxn}$.

The impulse responses for the model are calculated by using the [H], [A] and [B] matrices taken from the state space model as shown in equations (13) and (14) as

$$g(t) = [H]e^{[A]t}[B]. \tag{56}$$

The matrices [G1], [G2] and [G3] are multiplied with the simulation force to compute the displacement response, as shown in equation (1) of Chapter 2, at the 1st, 2nd and 3rd DOF's respectively. Inverse of matrices [G1], [G2] and [G3], as shown in equation (6), is used to reconstruct the forces. Greens function matrices are ill-conditioned and regularization is applied for the estimation of the force. Singular value decomposition as mentioned in equation (7), of Chapter 2, for [G1], [G2] and [G3] matrices is done to get the left singular vectors of matrix $[U] \in \mathbb{R}^{nxn}$, the right singular vectors of matrix $[V] \in \mathbb{R}^{nxn}$ and the diagonal matrix of singular values $[\sum] \in \mathbb{R}^{nxn}$, and these are used along with the computed displacement values for the purpose of reconstructing the force as shown in equation (8), of Chapter 2.

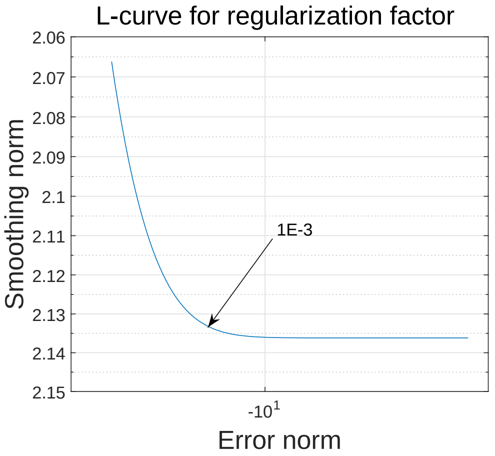

Figure 6. Graph of L-curve showing regularization factor (α) of 1E-3 on the plot of smoothing norm $\|[L][F]\|$ versus error norm $\|[G][F]-[S]\|$

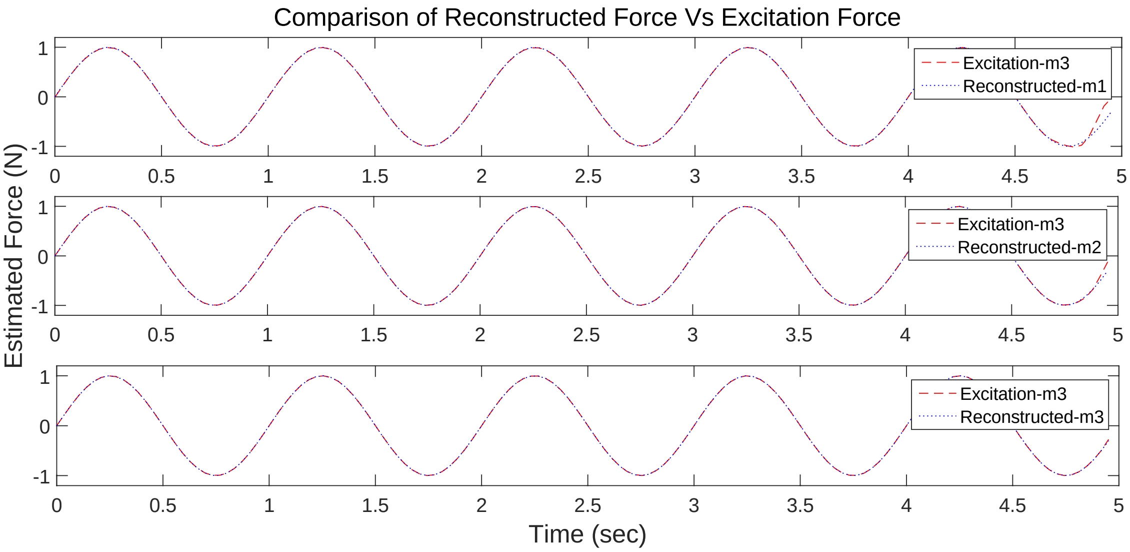

Figure 7. Actual versus reconstructed force simulation using deconvolution method. Regularization factor (α) used is 1E-3, excitation force applied at location m_3 and response measured at m_1, m_2 and m_3

The regularization factor is determined from the L-Curve, Figure 6, by plotting smoothing norm versus error norm. The plot of smoothing norm versus error norm as shown in equation (9), of Chapter 2, gives a regularization, α, factor of value, 1E-3, at the point where the curve gets the L-shape. Figure 7, show the comparison of simulation results of excitation and reconstructed force by the deconvolution method.

3.1.2 Reconstruction using Kalman filter RLS

The excitation force, for the numerical case study, is applied at the 3rd DOF and responses are measured at all the three (3) DOF's making it a single input and multi-output (SIMO) system. The vibration responses, as displacement, are computed using equation (17) on Chapter 2, at all the three (3) DOF's. These vibration responses are used to compute the estimated reconstructed force. The process and measurement noise co-variances, Q and R, were kept at 1.0E-6, while the error co-variance values, P and P_b, were kept at a high initial value of 1.0E8. The estimation process was seen to be largely affected by the fading factor, γ, which was inituively kept at the value of 7.7E-1 as this gave the best reconstruction of the excitation force. Figure 8, show the comparison of graphs for the reconstructed force versus the excitation force.

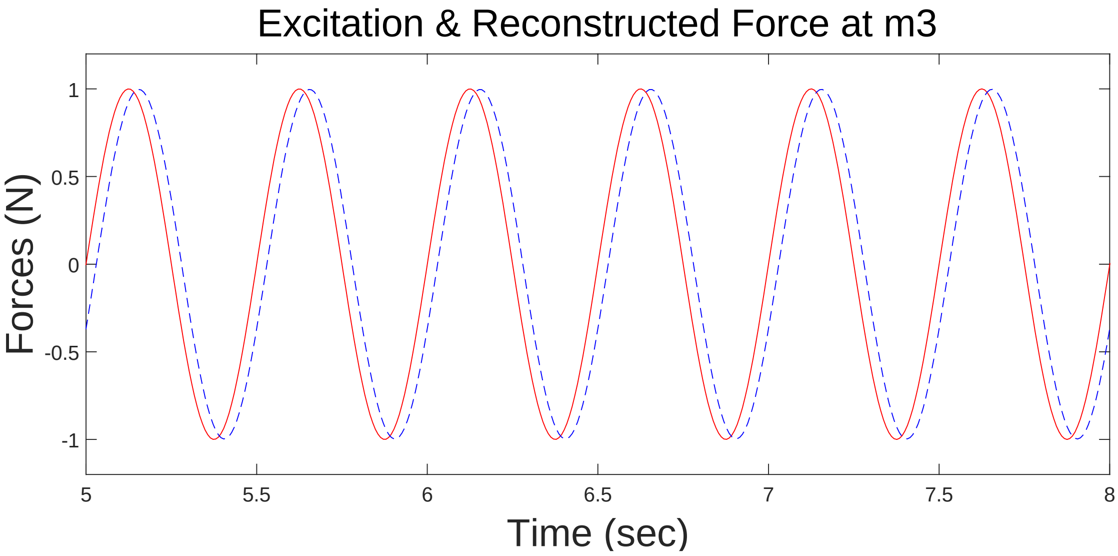

Figure 8. Actual (red) versus reconstructed (blue) force using Kalman filter RLS. Values used are γ- fading factor of 7.7E-1, Q and R of 1.0E-6, and error co-variance P and P_b of 1.0E8.

3.1.3 Augmented Kalman Filter

Similar to the methods explained in the previous sections, force is applied at the 3rd DOF and the vibration response is taken from all the three (3) DOF's making it a single input and multi-output (SIMO) system. In this numerical simulation as one the three locations of vibration measurement and that of the location application of the excitation force coincides at the 3rd DOF, thus making this numerical case study for augmented Kalman filter a collocated measurement scenario.

While the process and measurement noise co-variances, Q and R, were kept at 1.0E-6, the error co-variance, P, value was kept at a high initial value of 1.0E8. The reconstruction for the excitation force was very sensitive to the choice of co-variance, S, and this value was computed from the L-curve as 1.0E15. Figure 9, shows the comparison of graphs for the reconstructed force and the actual excitation force. Figure 10, shows the L-curve plot for calculating the regularization factor. The regularization factor converges on the smoothing norm of the graph and reconstruction of the excitation force with the regularization factors of 1.0E11, 1.0E12, 1.0E13, 1.0E14, 1.0E15 etc. on the L-curve gives similar results of reconstruction in terms of phase and magnitude.

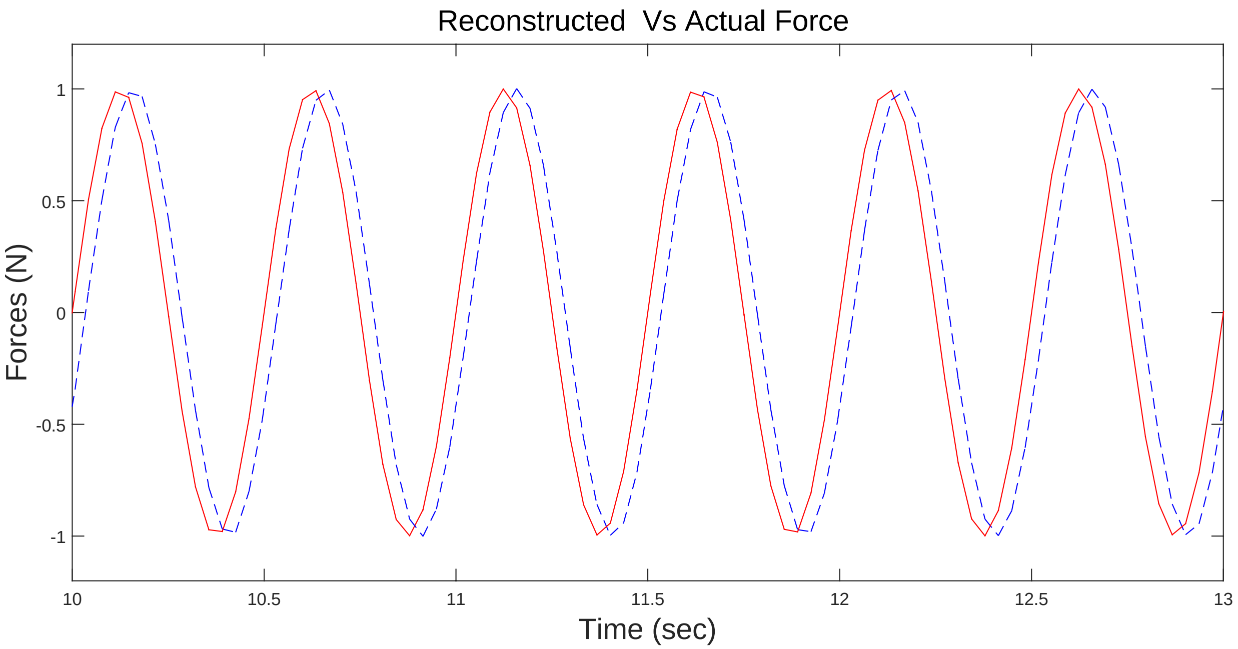

Figure 9. Actual (red) versus reconstructed (blue) force using augmented Kalman filter. Values used are Q, R and S of 1.0E-6, 1.0E-6 and 1.0E15, and error covariance P of 1.0E8

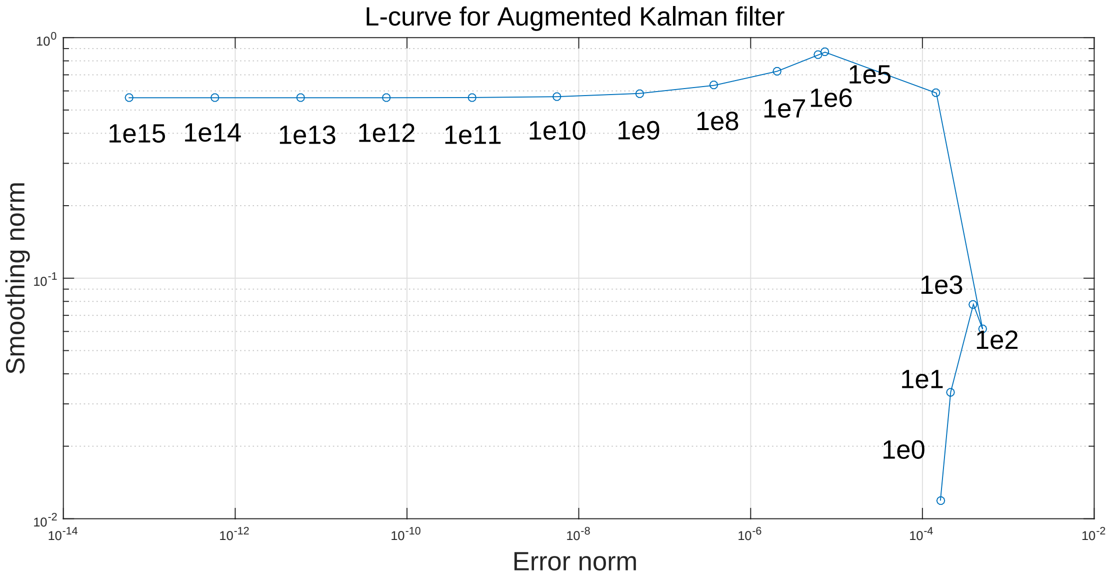

Figure 10. Graphical plot of L-curve for augmented Kalman filter. The smoothing curve converges and reconstruction using S values of 1.0E11, 1.0E12, 1.0E13, 1.0E14 and 1.0E15 are similar.

3.2 Observations at high frequency and low stiffness

The numerical case study was simultaneously done for two (2) other scenarios of high frequency excitation force and high stiffness to verify performance of the respective algorithms.

3.2.1 High frequency excitation

In this case an excitation force of higher frequency was applied to the system with parameters as shown in Table 1. The algorithms were tested by subjecting it to an excitation force of 1N at frequency of 30 Hz. Figure 11, shows the graph of the excitation applied for the simulation.

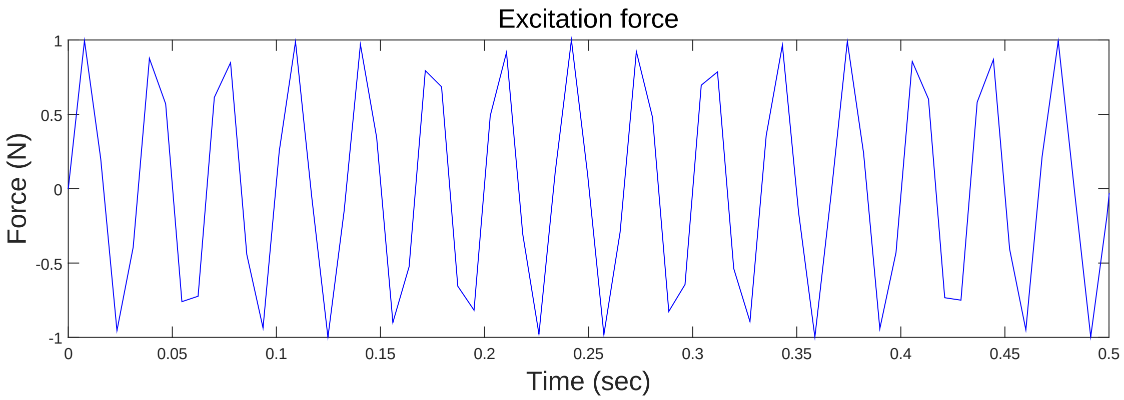

Figure 11. Sinusoidal excitation force with amplitude of 1N and frequency of 30 Hz

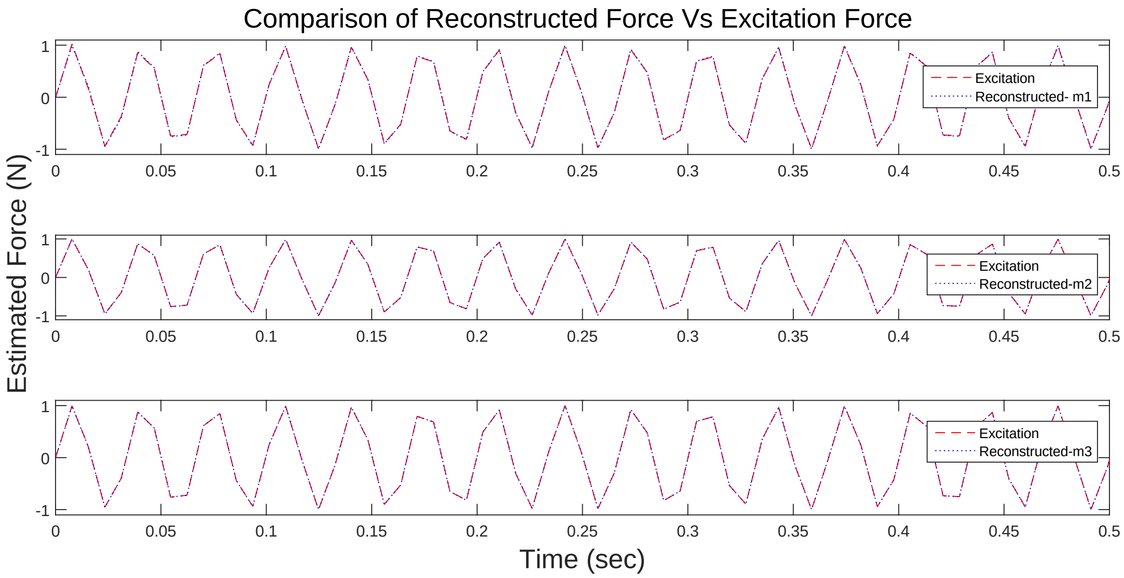

Figure 12. Actual versus reconstructed force simulation using deconvolution method with excitation force 1N at 30Hz. Regularization factor (α) used is 1E-3, excitation force applied at location m_3 and response measured at m_1, m_2 and m_3

The figures, Figure 12 – Figure 14, show the reconstruction versus excitation force from the simulation.

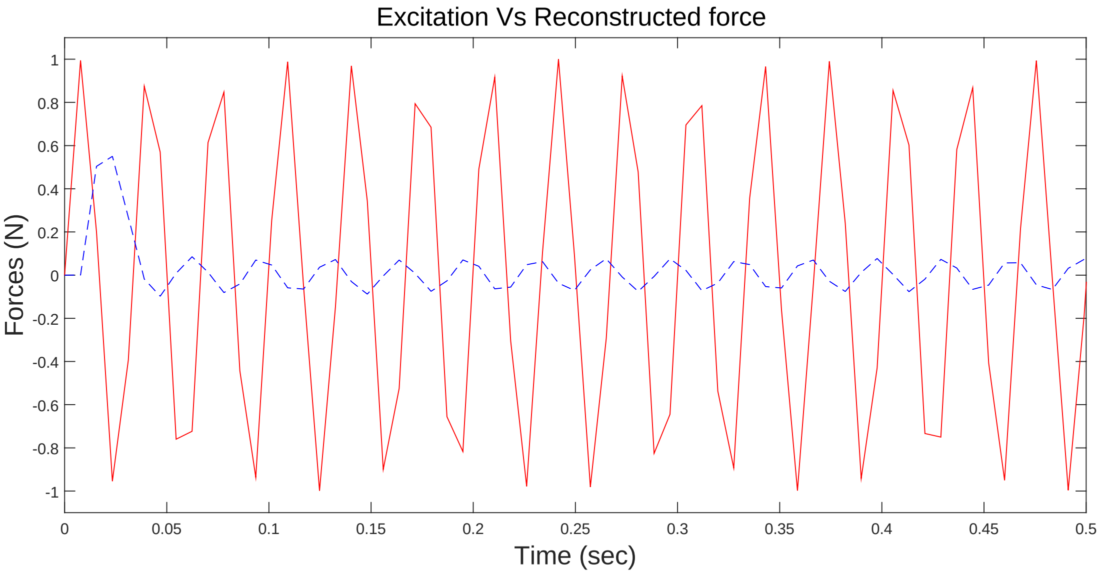

Figure 13. Actual (red) versus reconstructed (blue) force using Kalman filter RLS with excitation force 1N at 30Hz. Values used are γ- fading factor of 0.77, Q and R of 1.0E-6, and error co-variance P and P_b of 1.0E8

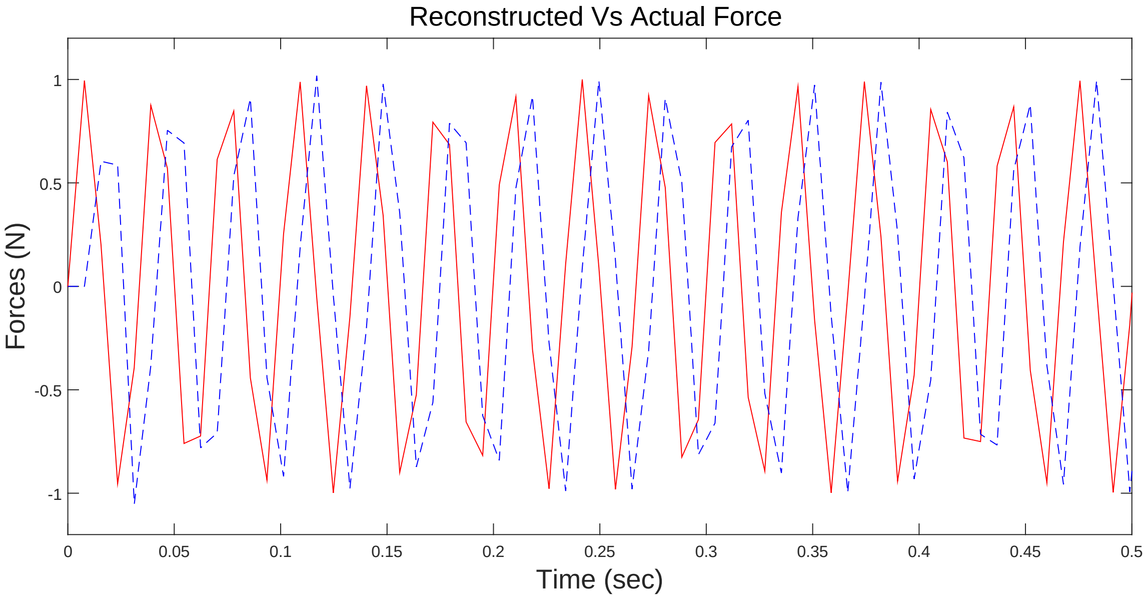

Figure 14. Actual (red) versus reconstructed (blue) force using augmented Kalman filter with excitation force 1N at 30Hz. Values used are Q, R and S of 1.0E-6, 1.0E-6 and 1.0E15, and error covariance P of 1.0E8

3.2.2 Low stiffness

In the case of low stiffness, the three (3) algorithms were tested at low stiffness values. Tabulated on Table 2 are the system parameters used for testing this scenario.

m_1	10kg	k_1	4000 N/m	c_1	100 N-sec/m
m_2	10kg	k_2	4000 N/m	c_2	100 N-sec/m
m_3	10kg	k_3	4000 N/m	c_3	100 N-sec/m

Table 2. Values of mass, stiffness and damping for a 3-DOF Mass-Stiffness-Damping model

The natural frequencies of this system with system parameters shown on Table 2 are $\omega_1 = 1.41$ Hz, $\omega_2 = 3.96$ Hz and $\omega_3 = 5.73$ Hz respectively. The figures, Figure 15 - Figure 17, show the graphical results of the outcome of the simulations. The reconstruction is proper for deconvolution method and augmented Kalman filter methods but with Kalman filter recursive least square the reconstructed force does not match the applied excitation force.

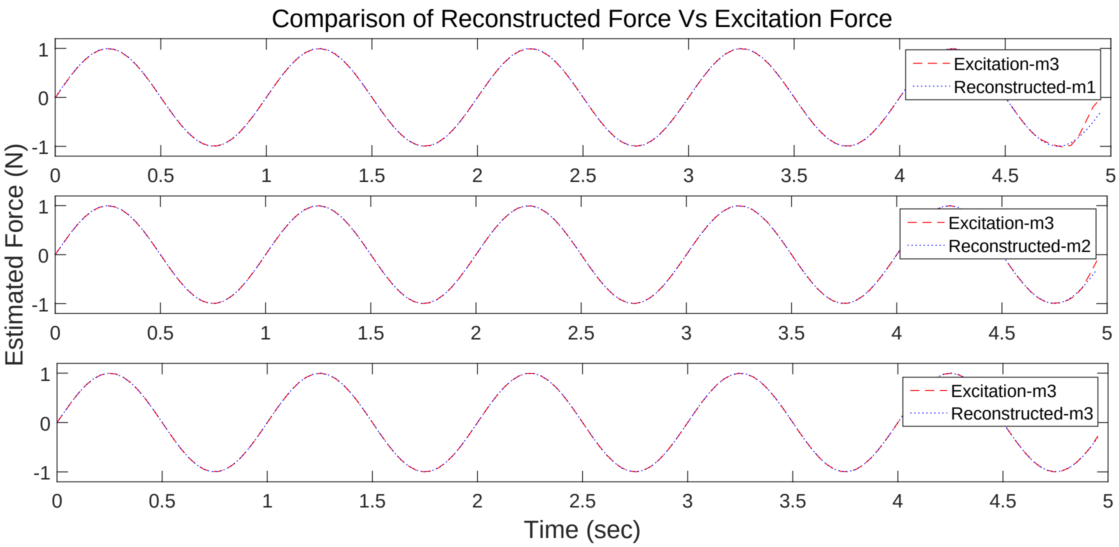

Figure 15. Actual versus reconstructed force simulation for lower stiffness using deconvolution method with excitation force 1N at 2Hz. Regularization factor (α) used is 1E-4, excitation force applied at location m_3 and response measured at m_1, m_2 and m_3

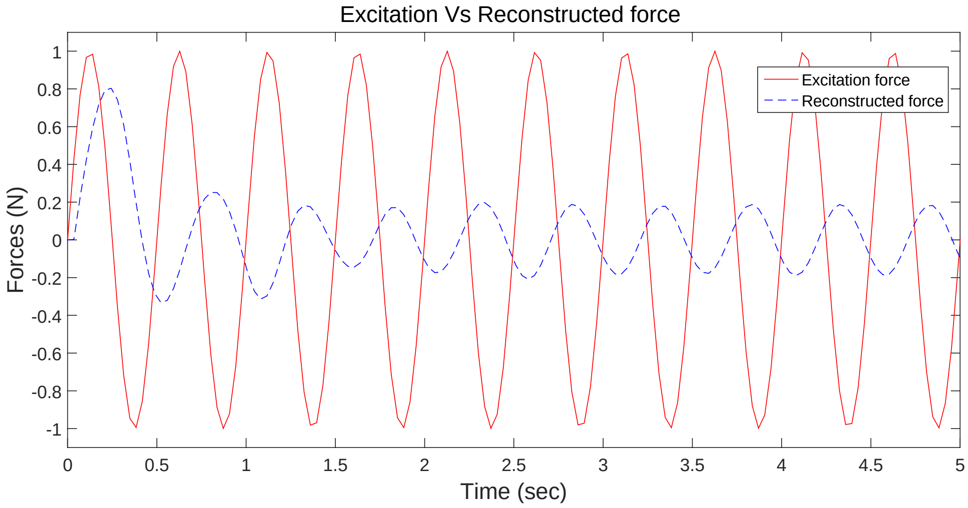

Figure 16. Actual (red) versus reconstructed (blue) force for lower stiffness using Kalman filter RLS with excitation force 1N at 2Hz. Values used are γ- fading factor of 0.77, Q and R of 1.0E-6, and error co-variance P and P_b of 1.0E8

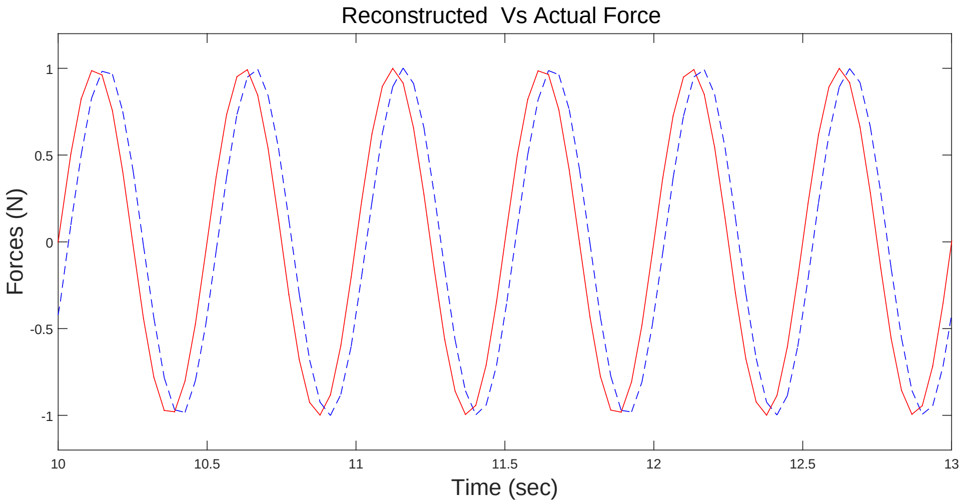

Figure 17. Actual (red) versus reconstructed (blue) force for lower stiffness using augmented Kalman filter with excitation force 1N at 2Hz. Values used are Q, R and S of 1.0E-6, 1.0E-6 and 1.0E15, and error covariance P of 1.0E8

3.3 Experimental Case Study

The experimental set-up for verifying and testing the force reconstruction algorithms developed on Matlab was done using a cantilever beam and shaker assembly. The algorithms tested for experimental case study were restricted to deconvolution method and augmented Kalman filter. As part of the experimental case study, Kalman filter RLS method was not applied, this was from the observations and outcome of numerical case study. The experimental model uses accelerometers for measuring the vibration response and a shaker with a load cell for applying an excitation force to the cantilever beam.

3.3.1 Experimental Set-up

The experimental set-up, as shown on Figure 18 consisted of three (3) main parts. First, an aluminum cantilever beam suspended from the edge of a vibration table.

Second, a shaker and signal generating assembly. The shaker used was Model K2007E01 by The Modal Shop. Figure 18 , shows the shaker used to apply dynamic force.

Third, three (3) accelerometers were used to measure the vibration responses on the cantilever beam. Figure 18 , shows the accelerometers marked as 1, 2 and 3 on the cantilever beam. The accelerometers used had the sensitivity of 1.085 mV/m/s^2, 1.050 mV/m/ s^2 and 1.062 mV/m/ s^2 respectively. The data recorded as acceleration from accelerometers was converted to velocity and then to displacement respectively by successively integrating it using FFT filtering once for each conversion. The integration methodology and codes were referenced from (Rune & Ventura, 2015).

Among others, a force hammer, Kistler 9722A500, was used for generating the modal parameters of the cantilever beam. The sensitivity and measuring range of the force hammer are 10.51 mV/lbf and 100lbf or 500N. CUTPRO® Simulation software installed on a Sony Vaio laptop, National Instruments digital and analog converter (DAC) were used for gathering, recording and analysis of the data.

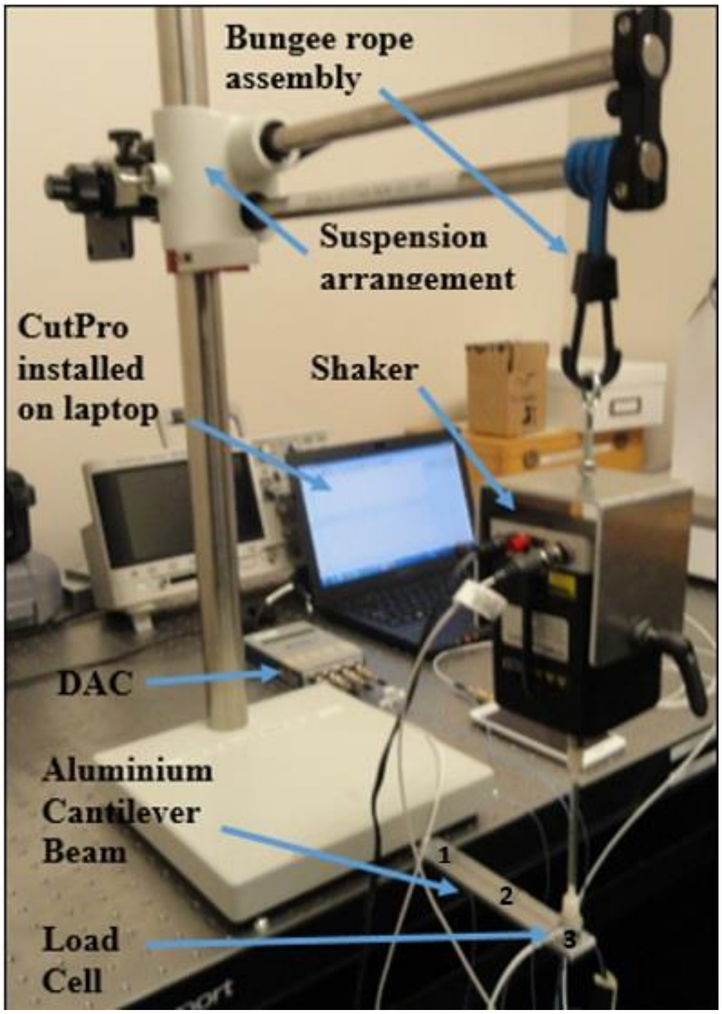

Figure 18. Experimental set-up for cantilever beam and shaker experiment. Location 1, 2 and 3 marked for accelerometers on the beam.

3.3.2 Modal analysis of cantilever beam

Modal analysis of the cantilever beam was conducted by using the CUTPRO® Simulation software, three (3) accelerometers and a force hammer. In this modal analysis of the beam (3) dominant modes were taken into consideration. The frequency response is shown on Figure 19. The mode shapes, $[\phi] \in \mathbb{R}^{3x3}$**,** measurements for the cantilever beam are

$$[\phi] = \begin{bmatrix} 0.242 & 1.972 & 3.731 \\ 2.346 & 4.867 & -0.753 \\ 5.517 & -2.936 & 1.939 \end{bmatrix}. \tag{57}$$

The matrix formed with the modal frequencies, $[\omega_n] \in \mathbb{R}^{1x3}$, of the three (3) dominant modes measured in Hz and converted to radians by multiplying with 2π are

$$[\omega_n] = 2\pi[119.108 \quad 885.441 \quad 2177.135]. \tag{58}$$

Here, ω_n represents modal frequencies of the three (3) dominant modes. Similarly, the damping ratio, $[\zeta_n] \in \mathbb{R}^{1x3}$, are

$$[\zeta_n] = [0.009 \quad 0.013 \quad 0.064]. \tag{59}$$

Here, ζ_n represents modal damping of the three (3) dominant modes. The applied excitation forces and the vibration responses were simultaneously recorded at the excitation frequencies of 1.0E2, 5.0E2, 6.0E2, 1.8E3, 2.1E3 and 2.5E3 Hz respectively.

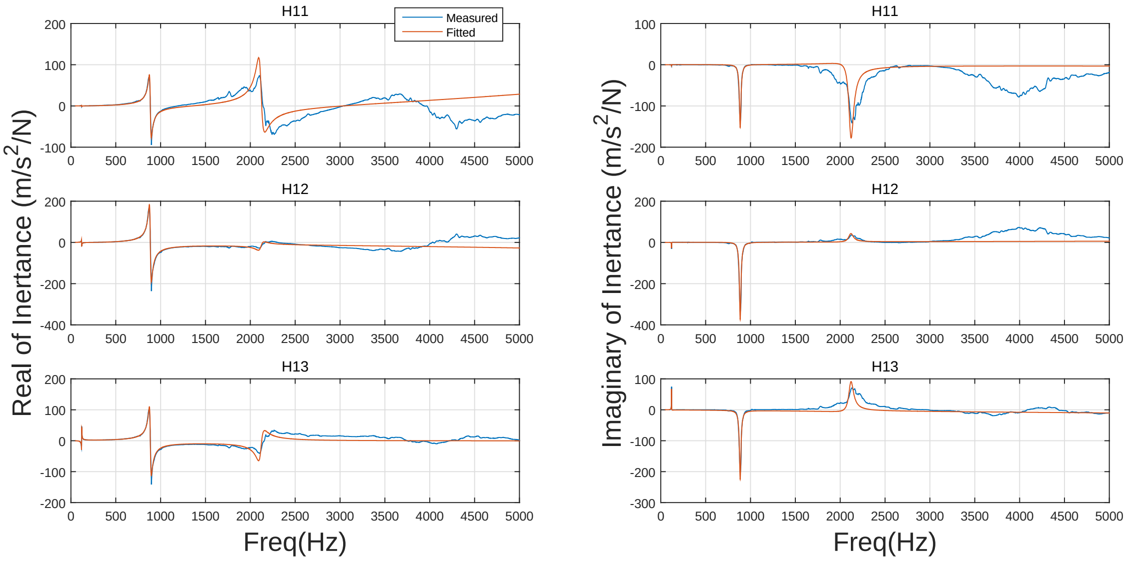

Figure 19. Real & Imaginary part of frequency response function for cantilever beam

The reason behind the choice of the mentioned frequencies for the excitation force was for having a good representation of sample data for testing around the natural frequencies of the 1st, 2nd and 3rd dominant modes of 119.108, 885.441 and 2177.135 Hz respectively.

3.3.3 Deconvolution method algorithm testing

In order to test the deconvolution method, the impulse responses were first computed in terms of the modal parameters by the formula [Rune Ventura, 2015] for impulse response function as

$$g(b,a,t) = \sum_{r=1}^{3} \phi_{br}\, \phi_{ar} \left[\frac{e^{\lambda_r t} - e^{\lambda_r^* t}}{\lambda_r - \lambda_r^*}\right]; b = 1 \text{ and } a = 1,2,3. \tag{60}$$

λ_r and λ_r^* are the two complex poles corresponding to each mode as

$$\lambda_r = -\zeta_r\omega_r + i\omega_r\sqrt{1-\zeta_r{}^2} \text{ and } \lambda_r^* = -\zeta_r\omega_r - i\omega_r\sqrt{1-\zeta_r{}^2}. \tag{61}$$

Using the impulse response function formulas, the impulse responses measured at the 3 (three) DOF's due a unit impulse applied at the 1st DOF are as

$$g(1,1,t) = \sum_{r=1}^{3} \phi_{1r}\,\phi_{1r}\left[\frac{e^{\lambda_r t} - e^{\lambda_r^* t}}{\lambda_r - \lambda_r^*}\right], \tag{62}$$

$$g(1,2,t) = \sum_{r=1}^{3} \phi_{1r}\,\phi_{2r}\left[\frac{e^{\lambda_r t} - e^{\lambda_r^* t}}{\lambda_r - \lambda_r^*}\right] \tag{63}$$

and

$$g(1,3,t) = \sum_{r=1}^{3} \phi_{1r}\,\phi_{3r}\left[\frac{e^{\lambda_r t} - e^{\lambda_r^* t}}{\lambda_r - \lambda_r^*}\right]. \tag{64}$$

The values of ϕ_{br}, ϕ_{ar}, ω_r and ζ_r were taken from equations (57), (58) and (59) respectively and the impulse responses for the time steps of $\Delta t, 2\Delta t, 3\Delta t$ till $n\Delta t$ were computed. The value for n in $n\Delta t$ is 514 and represents the total number of steps. The parameters of the experimental data are as

Parameter	Values
Sampling Frequency	25600 Hz
Total time samples used in force estimation	514

Table 3. Data parameters for deconvolution method

The impulse response values of $g(1,1,t)$, $g(1,2,t)$ and $g(1,3,t)$ are used to compute the Green's function matrices of [G1], [G2] and [G3] for the 3 (three) DOF's. The excitation force was applied by the shaker at the location of the third (3rd) DOF. The reconstruction of the force at the location of the first (1st) DOF was done with the vibration measured by the accelerometer at the first (1st) DOF. Similarly, for the second (2nd) and the third (3rd) DOF, with the vibration measurements recorded by the accelerometers at the second (2nd) and the third (3rd) DOF locations respectively. Singular values decomposition was done for the matrices [G1], [G2] and [G3], as shown in equation (5), of Chapter 2, and also the reconstruction of the excitation force was computed, as shown in equation (8) of Chapter 2. Ill-conditioning of [G1] and [G2] matrices was handled by removing the very low singular values by applying regularization factor. This regularization factor was computed from the L-Curve. The value of 1E-7 was taken as the regularization factor, from L-curve, shown on Figure 20. The arms of the L-curve merged at the point of coincidence the values of 1.0E-3, 1.0E-4, 1.0E-5, 1.0E-6 and 1.0E-7, the value of 1.0E-7 was intuitively chosen as the regularization factor for regularization.

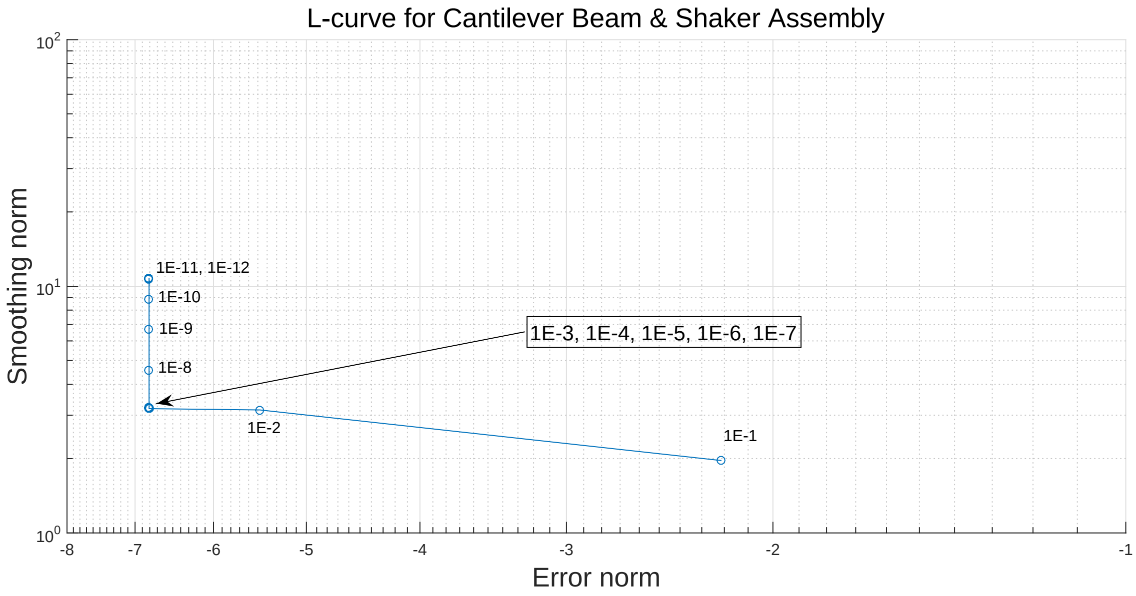

Figure 20. Graph of L-curve showing regularization factor (α) of 1E-7 on the plot of smoothing norm $\| [\mathbf{L}][\mathbf{F}] \|$ versus error norm $\| [\mathbf{G}][\mathbf{F}] - [\mathbf{S}] \|$

No regularization was applied at the 3rd DOF. The figures, Figure 21 - Figure 26 provides the graphs for comparison of the excitation and reconstructed forces at the frequencies of 1.0E2, 5.0E2, 6.0E2, 1.8E3, 2.1E3 and 2.5E3 Hz.

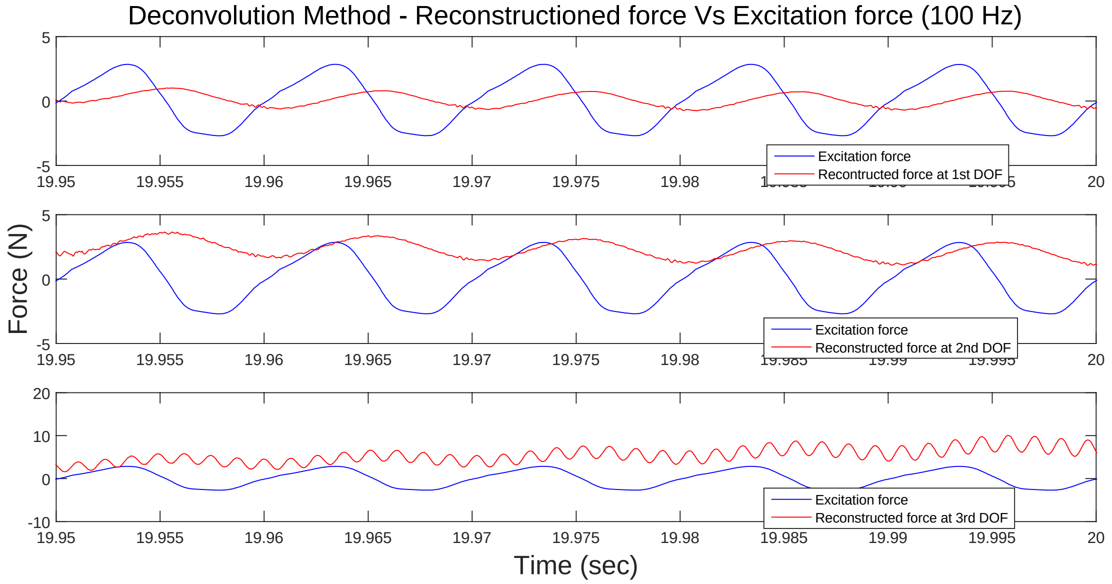

Figure 21. Actual versus reconstructed force simulation for lower stiffness using deconvolution method with excitation force at 100Hz. Regularization factor (α) used is 1E-7, excitation force applied at 3rd DOF and response measured at 1st, 2nd and 3rd DOF locations.

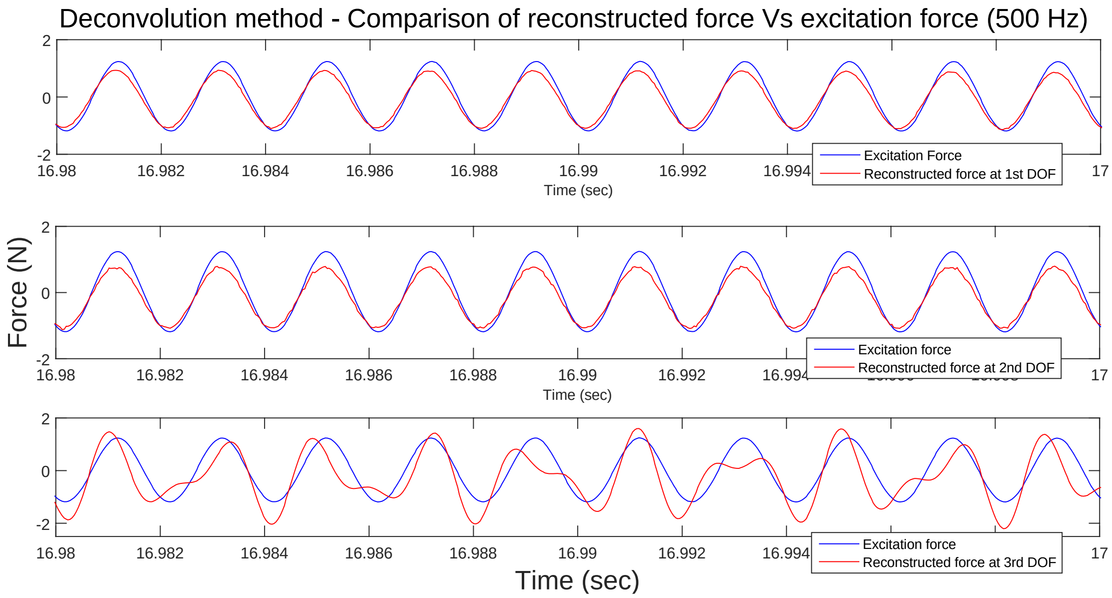

Figure 22. Actual versus reconstructed force simulation for lower stiffness using deconvolution method with excitation force at 500Hz. Regularization factor (α) used is 1E-7, excitation force applied at 3rd DOF and response measured at 1st, 2nd and 3rd DOF locations.

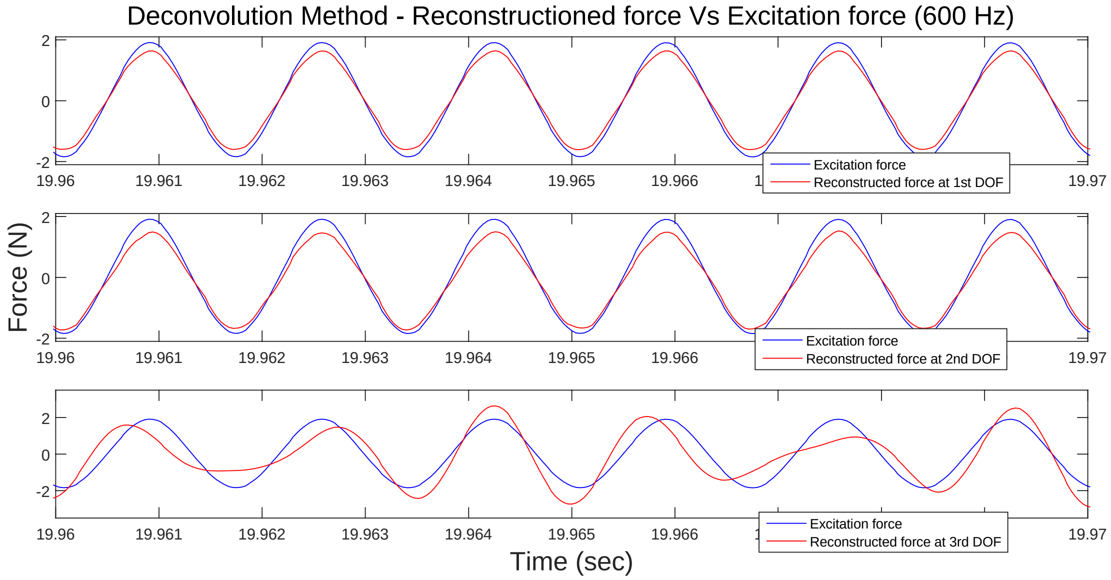

Figure 23. Actual versus reconstructed force simulation for lower stiffness using deconvolution method with excitation force at 600Hz. Regularization factor (α) used is 1E-7, excitation force applied at 3rd DOF and response measured at 1st, 2nd and 3rd DOF locations.

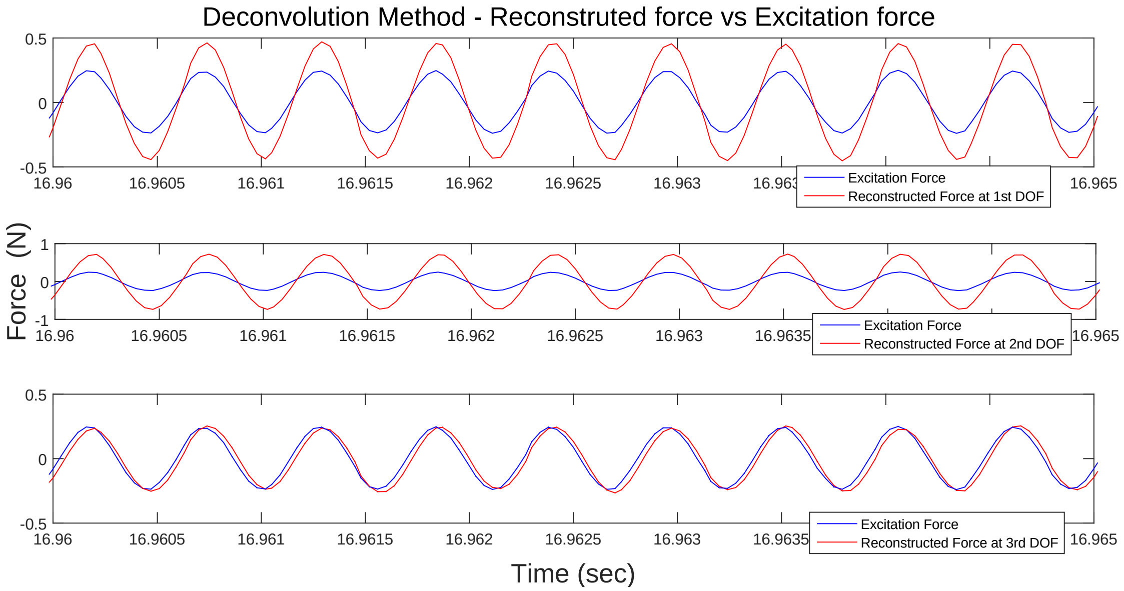

Figure 24. Actual versus reconstructed force simulation for lower stiffness using deconvolution method with excitation force at 1800Hz. Regularization factor (α) used is 1E-7, excitation force applied at 3rd DOF and response measured at 1st, 2nd and 3rd DOF locations.

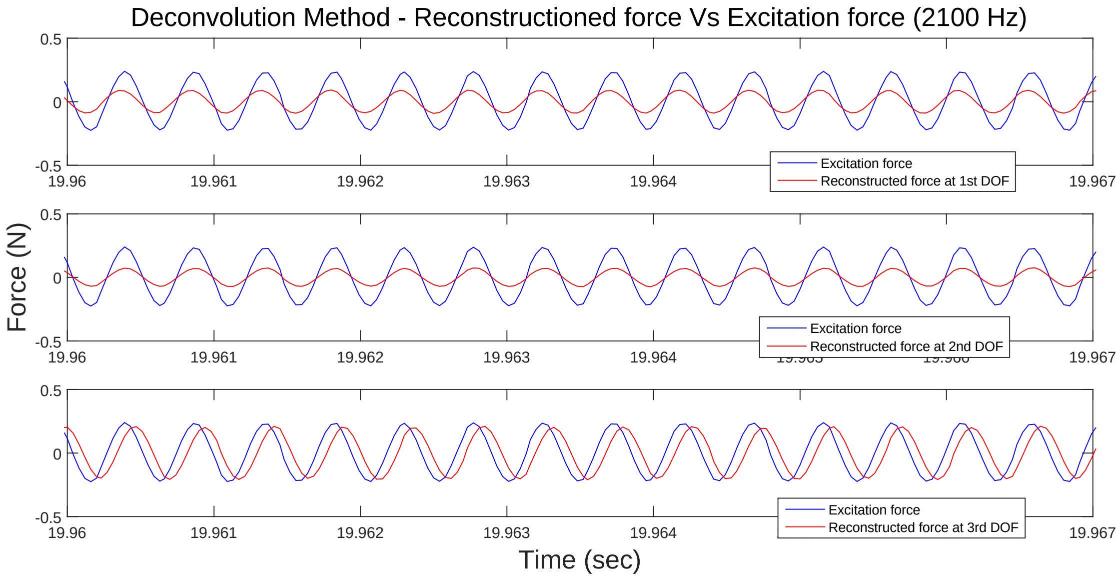

Figure 25. Actual versus reconstructed force simulation for lower stiffness using deconvolution method with excitation force at 2100Hz. Regularization factor (α) used is 1E-7, excitation force applied at 3rd DOF and response measured at 1st, 2nd and 3rd DOF locations.

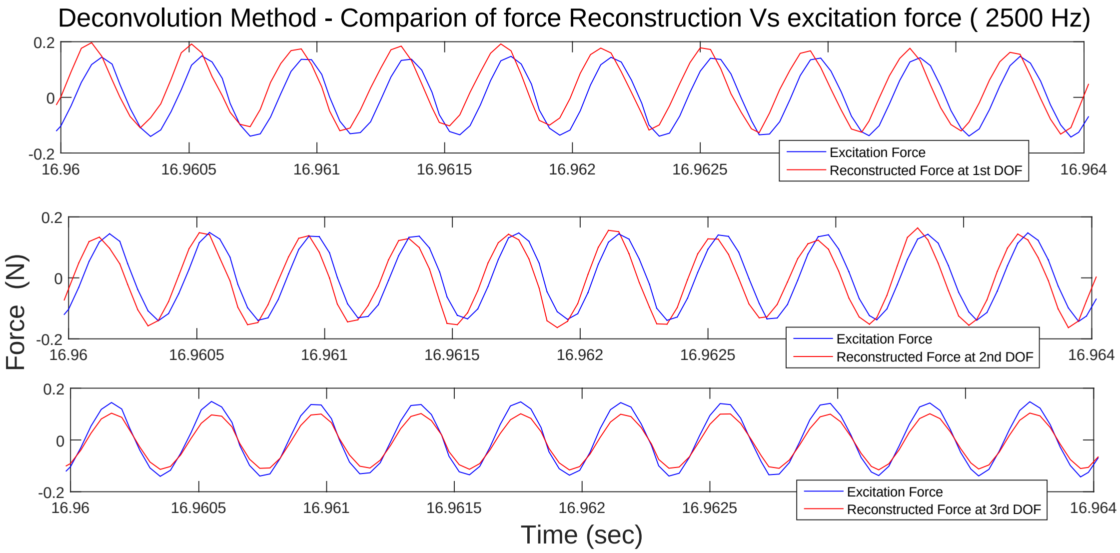

Figure 26. Actual versus reconstructed force simulation for lower stiffness using deconvolution method with excitation force at 2500Hz. Regularization factor (α) used is 1E-7, excitation force applied at 3rd DOF and response measured at 1st, 2nd and 3rd DOF locations.

Reconstruction for the excitation force was found to be good at the frequencies of 5.0E2, 6.0E2 and 2.5E3 Hz but not adequate for the frequencies of 1.8E3 and 2.1E3 Hz. The fitment of the fitted and the actual FRF is not of fair quality as shown on Figure 19, and this resulted in inadequate reconstruction at frequencies of poor fitment. The fitted FRF values were used for the deconvolution method for maintaining consistency with the augmented Kalman filter method. The reconstruction of the excitation forces with the excitation frequencies closer to the natural frequencies of the dominant modes of the beam were very poor due to the effect of resonance.

3.3.4 Augmented Kalman filter algorithm testing

In order to test the augmented Kalman filter method, both the cases of collocated and non-collocated measurement scenarios were tested. The position of the accelerometers and the shaker for the collocated and non-collocated scenarios are shown on the figures, Figure 27 and Figure 28, respectively.

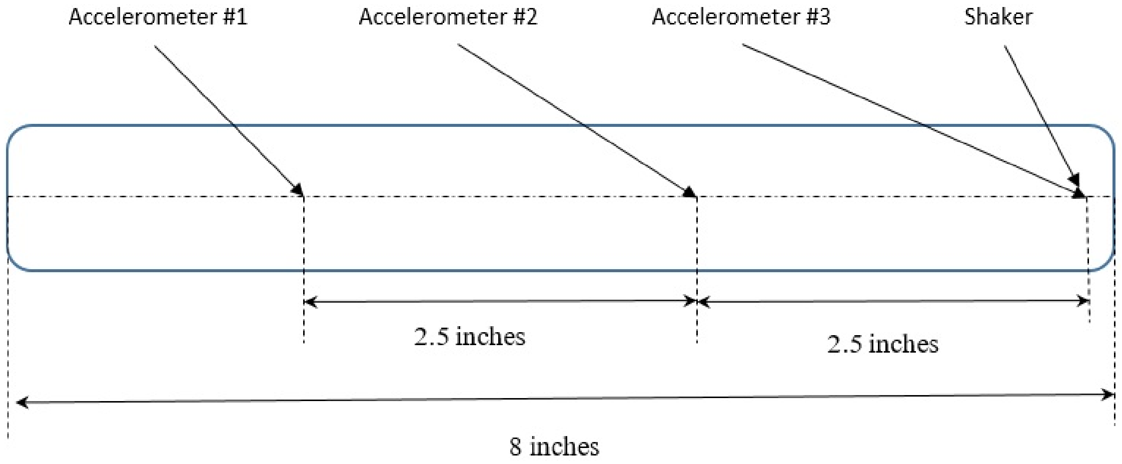

Figure 27. Position of accelerometers on cantilever beam for collocated measurement scenario. Overhang of cantilever is 6inches and accelerometer kept 2.5 inches apart.

In both the cases three (3) accelerometers were used to measure the vibration response. In the case of collocated scenario, one (1) of the accelerometers was placed at the location where the excitation force was applied.

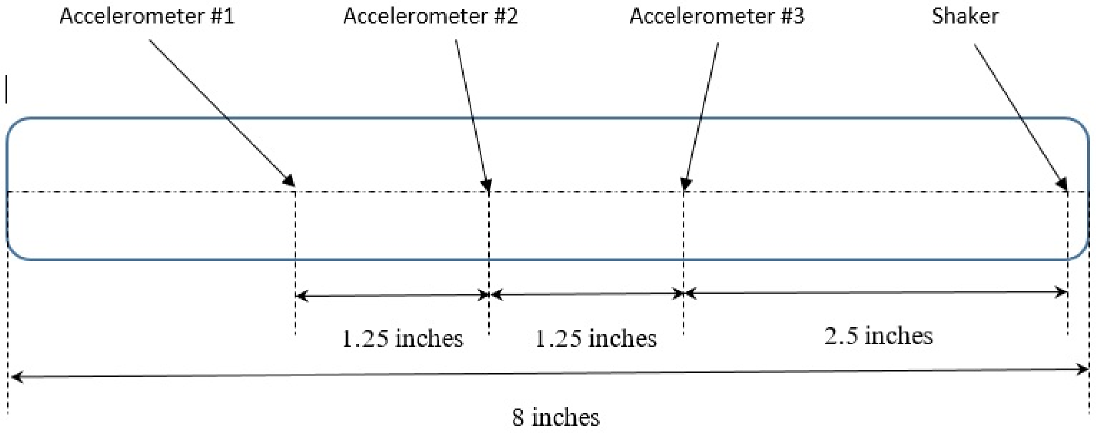

Figure 28. Position of accelerometers on cantilever beam for non-collocated measurement scenario. 6 inches overhang and accelerometers kept 1.25 inches apart.

On the other hand, for the non-collocated scenario, experiment was conducted with all the three (3) accelerometers placed away from the location where the excitation force was applied.

3.3.4.1 Collocated measurement scenario

In this scenario, the process starts with generating the state space model with the measured values of mode shapes matrix, $[\phi] \in \mathbb{R}^{3x3}$, natural frequencies, ω_n and damping ratios, ζ_n. The matrices constructed for the state space model are

$$[A] = \begin{bmatrix} 0_{3x3} & I_{3x3} \\ -[\omega_n{}^2] & -[2\zeta_n\omega_n] \end{bmatrix};\ [B] = \begin{bmatrix} 0_{3x3} \\ [\phi]^T \end{bmatrix};\ [C] = \begin{bmatrix} I_{3x3} & 0_{3x3} \\ 0_{3x3} & 0_{3x3} \end{bmatrix} \text{ and } [D] = 0. \tag{65}$$

The matrices [A], [B], [C] and [D] are the state matrix, input matrix, output matrix and feed through matrix respectively. The values of the components in the matrices are computed as

$$[\omega_n{}^2] = \begin{bmatrix} \omega_1{}^2 & 0 & 0 \\ 0 & \omega_2{}^2 & 0 \\ 0 & 0 & \omega_3{}^2 \end{bmatrix}, \tag{66}$$

$$[2\zeta_n\omega_n] = \begin{bmatrix} 2\zeta_1\omega_1 & 0 & 0 \\ 0 & 2\zeta_2\omega_2 & 0 \\ 0 & 0 & 2\zeta_3\omega_3 \end{bmatrix}. \tag{67}$$

The values for the natural frequencies ω_1, ω_2 and ω_3 of the 3 dominant modes in equation (66), are $2\pi * 119.108$ rad/s, $2\pi * 885.441$ rad/s and $2\pi * 2177.135$ rad/s respectively. The values for $2\zeta_1\omega_1$, $2\zeta_2\omega_2$ and $2\zeta_3\omega_3$ in equation (67) are $2 * 0.009 * 2\pi * 119.108$, $2 * 0.013 * 885.441$ and $2 * 0.064 * 2177.135$ respectively. 0_{3x3}, I_{3x3} and $[\phi]^T$ are respectively the three (3) by three (3) diagonal matrix of zeros, identity matrix and the transpose of the mode shape, $[\phi]$, matrix.

Next, from the discrete time state space model in equations (35) and (36) of Chapter 2, $[\emptyset] \in \mathbb{R}^{6x6}$ and $[\Gamma] \in \mathbb{R}^{6x3}$, matrices are used to create the augmented matrices, $[A_a]$ and $[G_a]$, as shown on equation (40) of Chapter 2. The values for the matrices, $[G_a]$ and $[A_a]$, are

$$[G_a] = \begin{bmatrix} I_{3x3} & 0_{3x3} & 0_{3x3} \\ 0_{3x3} & 0_{3x3} & 0_{3x3} \\ 0_{3x3} & 0_{3x3} & 0_{3x3} \end{bmatrix}, \tag{68}$$

$$[A_a] = \begin{bmatrix} [\emptyset] & [\Gamma] \\ 0_{3x6} & I_{3x3} \end{bmatrix}. \tag{69}$$

The co-variance matrices of, [Q], as shown on equation (41), and [R], as shown on equation (42) from Chapter 2, of the augmented Kalman filter takes the form

$$[Q] = (10^{-3}) I_{6x6}\ , \tag{70}$$

$$[\mathrm{R}] = (10^{-8})\mathrm{I}_{9\mathrm{x}9}.$$

The co-variance matrix, S, as shown on equation (43) from Chapter 2, takes the value of 1.0E15 and was calculated using the L-curve shown on Figure 29. The regularization factor converges on the smoothing norm on the L-curve at 1.0E15, 1.0E16, 1.0E17, 1.0E18, 1.0E19, 1.0E20, 1.0E21 and 1.0E23. Intuitively, 1.0E15 is taken as value for regularization factor.

$$[\mathrm{S}] = (10^{15})\mathrm{I}_{3\mathrm{x}3}\ . \tag{71}$$

The phenomenon of convergence of regularization factor on the smoothing norm on the L-curve for collocated measurements finds mention on literature published by researchers (E, Reynders, DeRoeck, Degrande, & G.Lombaert, 2012).

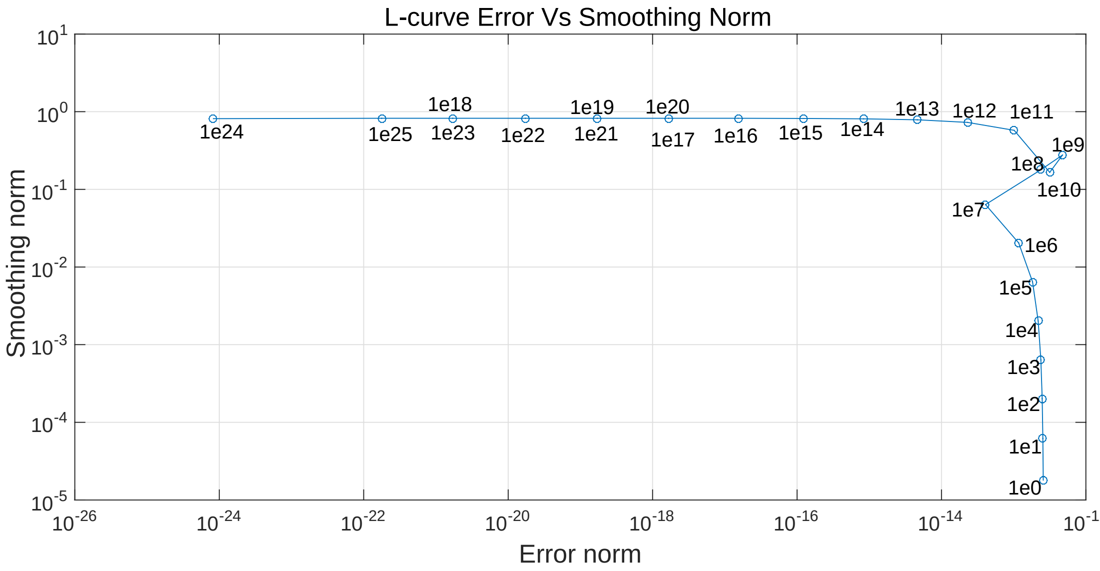

Figure 29. Graphical plot of L-curve for augmented Kalman filter. The smoothing curve converges and reconstruction using S values of 1.0E15, 1.0E16, 1.0E17, 1.0E18, 1.0E19, 1.0E20, 1.0E21, 1.0E22 and 1.0E23 are similar.

Finally, the augmented co-variance matrix,$[\mathrm{Q_a}]$ as shown on equation (49) from Chapter 2, takes the form

$$[\mathrm{Q_a}] = \begin{bmatrix} (10^{-3})\mathrm{I}_{6\mathrm{x}6} & 0_{6\mathrm{x}3} \\ 0_{3\mathrm{x}6} & (10^{15})\mathrm{I}_{3\mathrm{x}3} \end{bmatrix}. \tag{72}$$

The initial value for the time update of the states,$[\overline{\mathrm{X}}^{a}_{0|-1}]\ \in \mathbb{R}^{9}$ is set to zero and for the error covariance, $[P_{0|-1}] \in \mathbb{R}^{9\mathrm{x}9}$ it is set to a high number, 1.0E2 as

$$[\overline{\mathrm{X}}^{a}_{0|-1}] = [0_{1\mathrm{x}9}]^{\mathrm{T}}\ , \tag{73}$$

$$[P_{0|-1}] = (10^2)\mathrm{I}_{9x9} \quad . \tag{74}$$

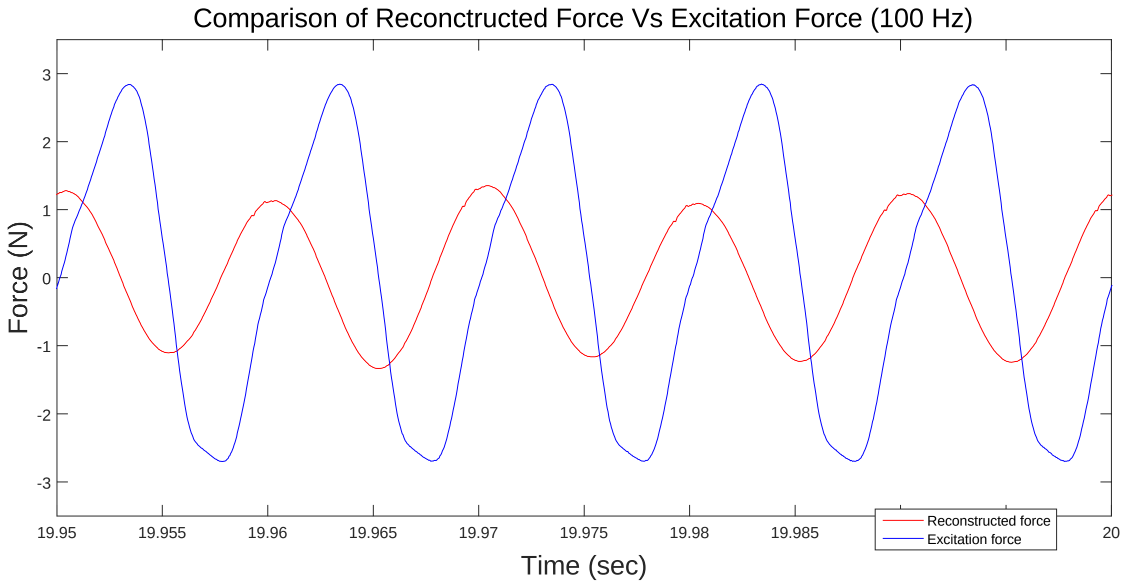

Figure 30. Actual versus reconstructed force using augmented Kalman filter with frequency of excitation force at 100 Hz. Values used are Q, R and S of 1.0E-3, 1.0E-8 and 1.0E15, and error covariance P of 1.0E2

The figures, Figure 30 - Figure 35, show the results of the force reconstruction at the excitation frequencies of 1.0E2, 5.0E2, 6.0E2, 1.8E3, 2.1E3 and 2.5E3 Hz respectively.

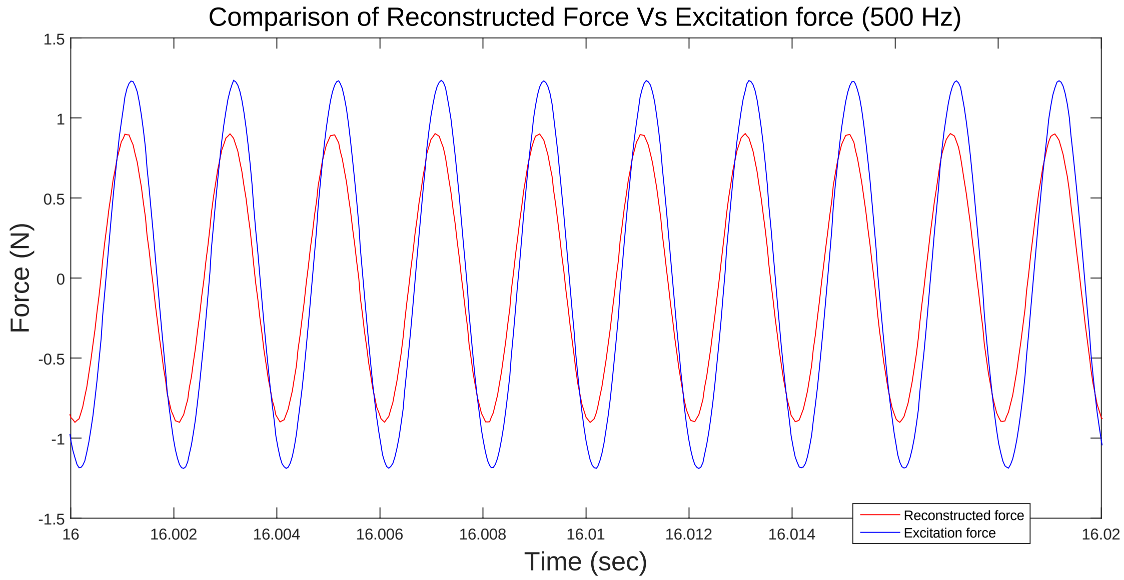

Figure 31. Actual versus reconstructed force using augmented Kalman filter with excitation force at 500 Hz. Values used are Q, R and S of 1.0E-3, 1.0E-8 and 1.0E15, and error covariance P of 1.0E2

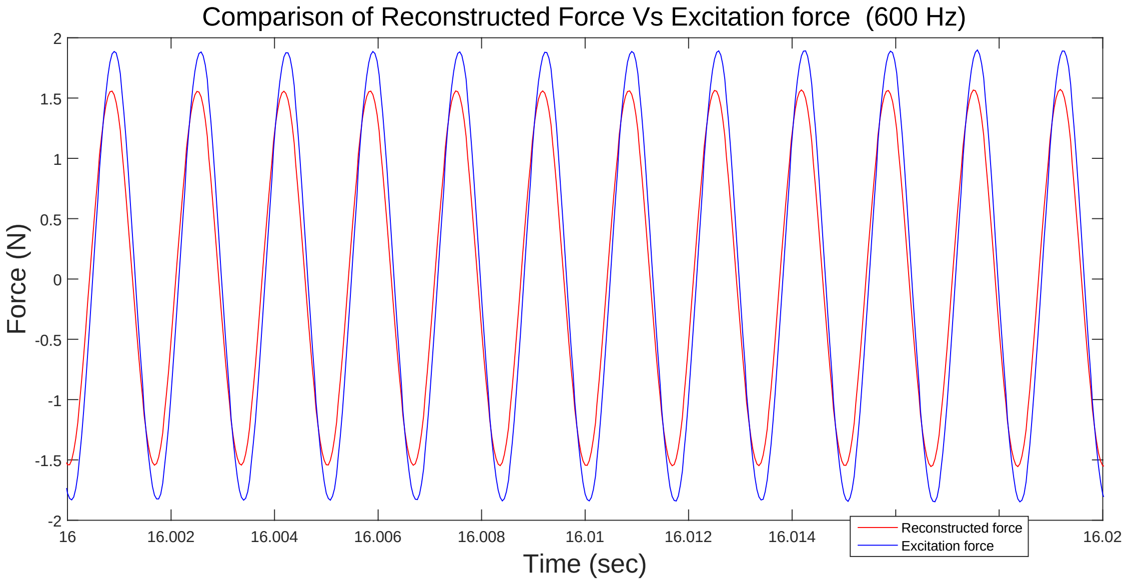

Figure 32. Actual versus reconstructed force using augmented Kalman filter with excitation force at 600 Hz. Values used are Q, R and S of 1.0E-3, 1.0E-8 and 1.0E15, and error covariance P of 1.0E2

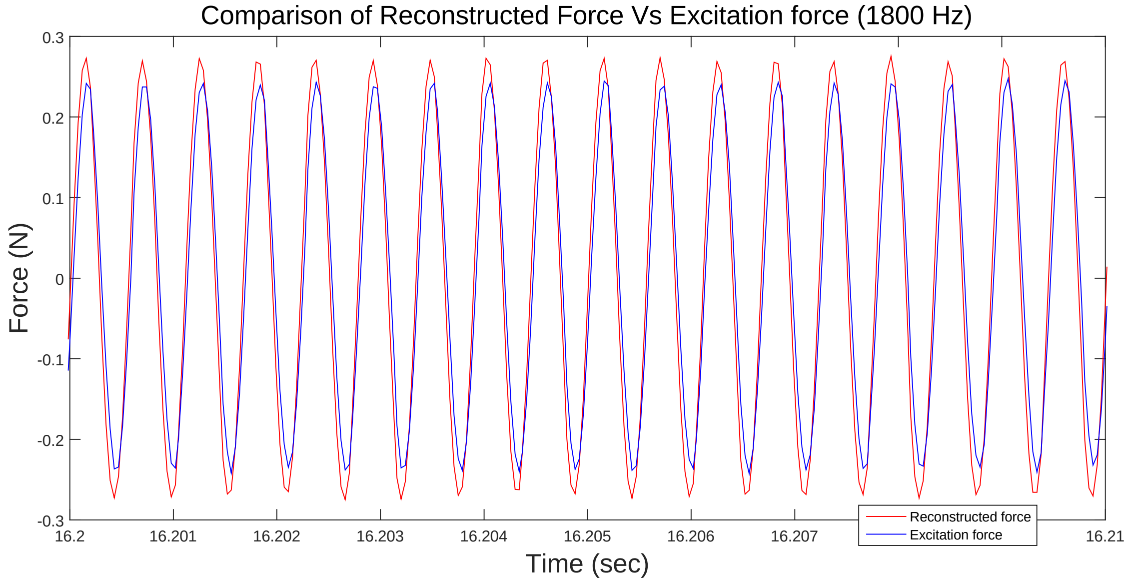

Figure 33. Actual versus reconstructed force using augmented Kalman filter with excitation force at 1800 Hz. Values used are Q, R and S of 1.0E-3, 1.0E-8 and 1.0E15, and error covariance P of 1.0E2

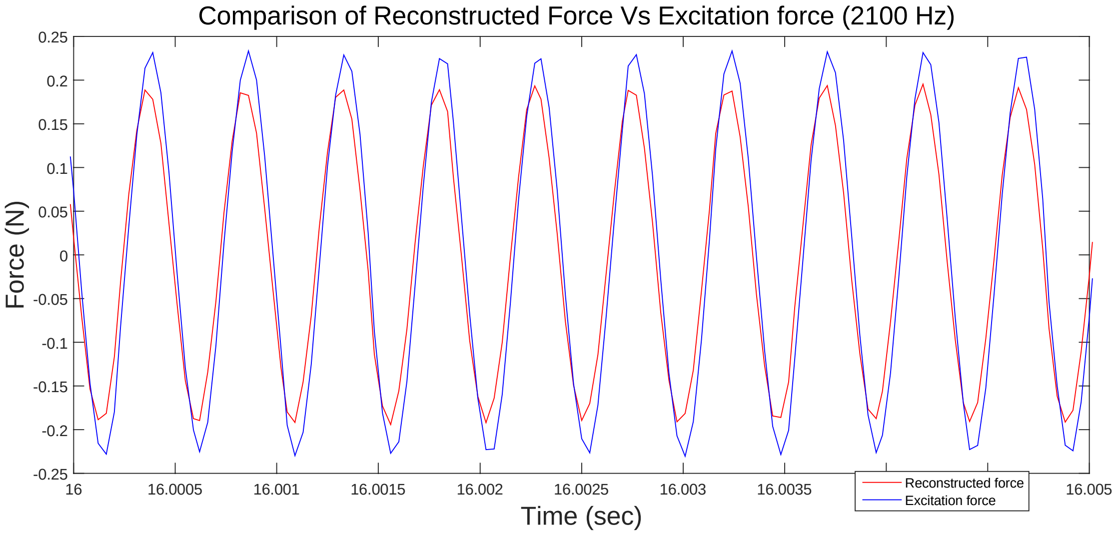

Figure 34. Actual versus reconstructed force using augmented Kalman filter with excitation force at 2100 Hz. Values used are Q, R and S of 1.0E-3, 1.0E-8 and 1.0E15, and error covariance P of 1.0E2

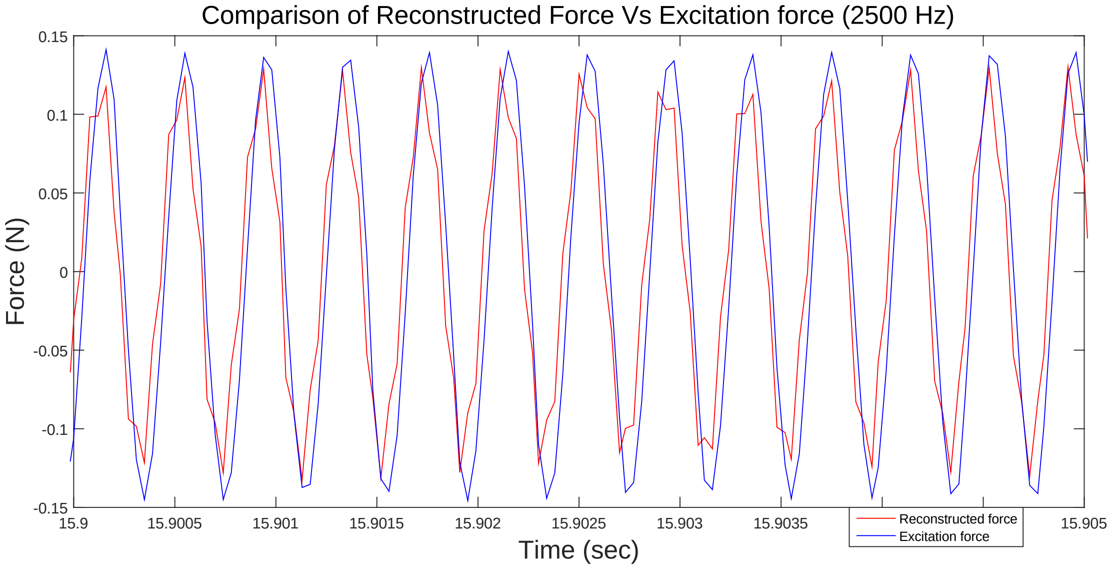

Figure 35. Actual versus reconstructed force using augmented Kalman filter with excitation force at 2500 Hz. Values used are Q, R and S of 1.0E-3, 1.0E-8 and 1.0E15, and error covariance P of 1.0E2

The reconstruction was poor for the excitation forces at excitation frequencies closer the natural frequencies of the beam due to the effect of resonance.

3.3.4.2 Non-collocated measurement scenario

In this case the same cantilever beam was tested with all the accelerometers away from the location of the application of the excitation force. This test was specifically carried out based on the findings in literature by authors [E, Reynders, DeRoeck, Degrande, G.Lombaert, 2012], on non-convergence of regularization factor for non-collocated measurements, to study the behavior of force reconstruction pattern and non-convergence of regularization factor values on the smoothing norm of the L-curve. Modal analysis was done for the cantilever beam again with the new placement, as shown on Figure 28, of the accelerometers. The mode shapes, $[\phi] \in \mathbb{R}^{\mathbf{3x3}}$ are

$$[\phi] = \begin{bmatrix} 0.187 & 1.596 & 3.360 \\ 1.172 & 4.138 & 3.809 \\ 2.686 & 4.820 & -0.682 \end{bmatrix}. \tag{75}$$

The natural frequencies, $[\omega_{\,n}] \in \mathbb{R}^{\mathbf{1x3}}$, of the three (3) dominant modes measured in Hz and converted to radians by multiplying with 2π are

$$[\omega_{\,n}] = 2\pi[125.991 \quad 934.534 \quad 2299.209]. \tag{76}$$

Similarly, the damping ratios, $[\zeta_{\,n}] \in \mathbb{R}^{\mathbf{1x3}}$ are

$$[\zeta_{\,n}] = [0.006 \quad 0.008 \quad 0.038]. \tag{77}$$

Figure 36, shows the frequency response function.

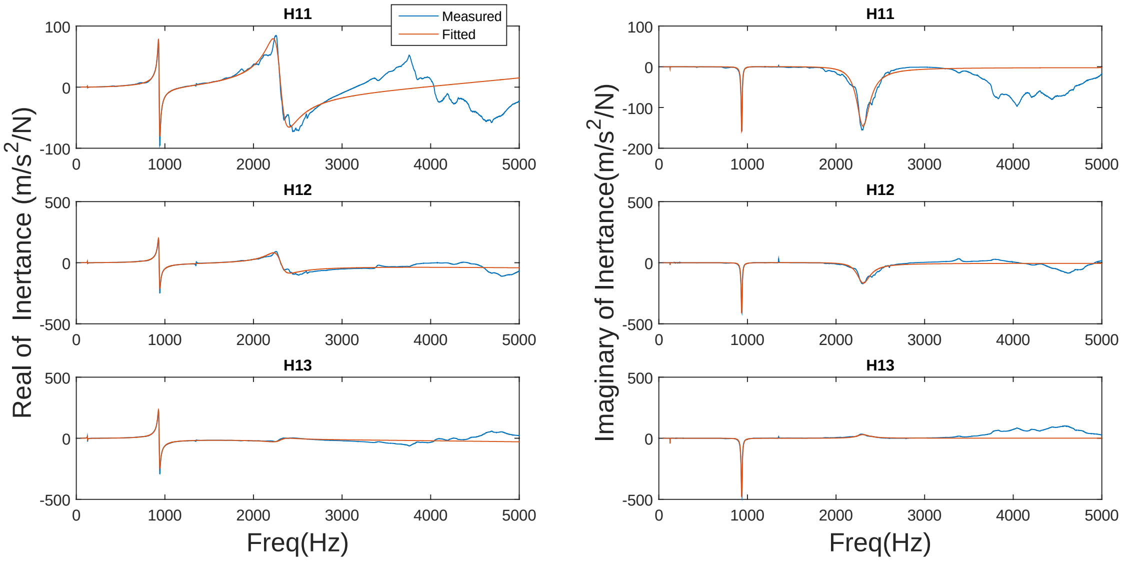

Figure 36. Real & Imaginary part of frequency response function for cantilever beam (non-collocated)

It was observed that the value of covariance matrix, [S], used for the collocated case was no longer giving similar results here in the case of non-collocated measurement. The regularization factor, on L-curve, did not converge on the smoothing norm (E, Reynders, DeRoeck, Degrande, & G.Lombaert, 2012) and the magnitude of the reconstructed force gradually kept on increasing with increasing value of the regularization factor. The best performance of reconstruction was at the value of 1.0E7.

Figure 37, shows performance of the reconstruction with the diagonal value of covariance matrix, [S], as 1.0E7. Figure 38, shows the L-curve with regularization values marked on it.

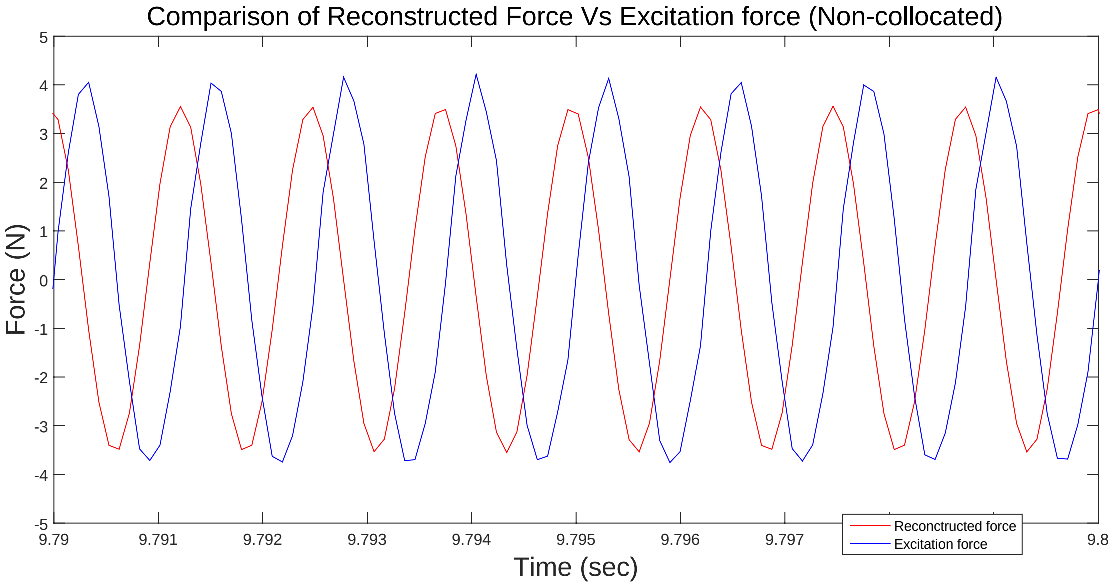

Figure 37. Actual versus reconstructed force using augmented Kalman filter for non-collocated measurement with excitation force at 500 Hz. Values used are Q, R and S of 1.0E-3, 1.0E-8 and 1.0E7, and error covariance P of 1.0E2

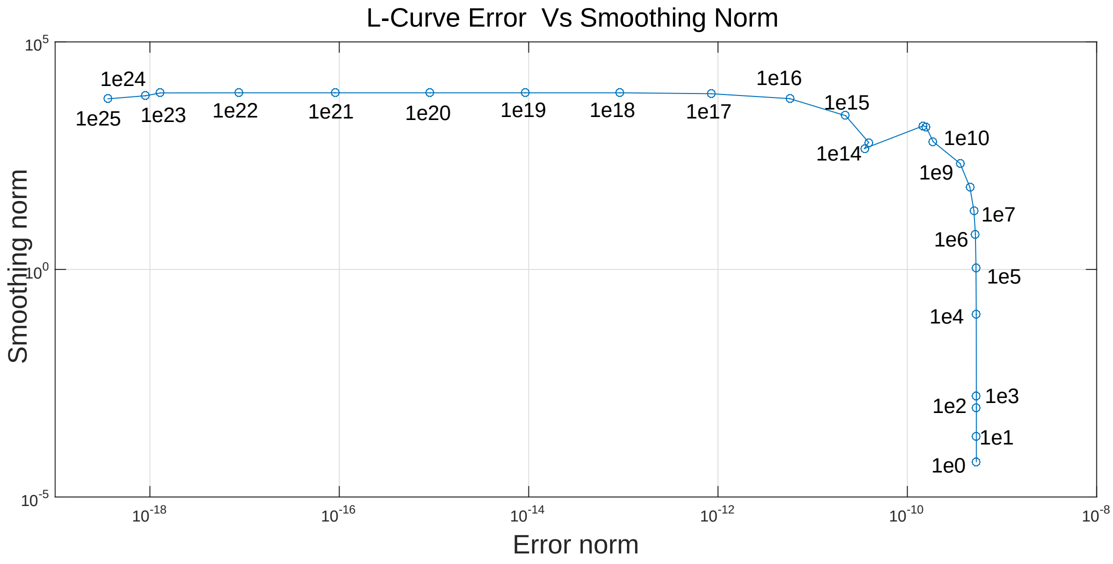

Figure 38. Graphical plot of L-curve for augmented Kalman filter. The regularization factor value does not converge on smoothing norm and the amplitude of reconstruction constantly increases. The best reconstruction is at 1.0E7

3.4 Observations on cantilever beam & shaker experiment

The analysis of results from the cantilever beam and shaker experiment provides the following observations.

1. The deconvolution method gives good results of force reconstruction from vibration measurements taken at points away from the location of impact after applying regularization.
2. The deconvolution method is suited for single-input single-output (SISO) scenario.
3. The deconvolution method shows poor reconstruction in cases of poor fitment between fitted to actual FRF.
4. The augmented Kalman filter method is suited for the single-input multi-output scenario.
5. The augmented Kalman filter method works best for the collocated measurement scenario.

Chapter 4

Forces reconstruction of cutting forces on CNC Machine

This chapter provides details on the experiments of milling operation conducted on a Computer Numerical Control (CNC) machine for the reconstruction of cutting forces. Commonly available CNC machines are 3 to 6-axis milling, lathe etc. machine, but in our case it was a 3-axis milling machine. The system model for the experiments, milling operation, was a multi-input multi-output (MIMO) system of cutting forces and vibration responses. Here, input and output to the system are respectively the cutting forces and vibration responses. The deconvolution method was not applied for the reconstruction of cutting forces on these experiments because it is more suited for single-input single-output (SISO) scenarios. Instead, the augmented Kalman Filter method was applied here for cutting force reconstruction on the experiments.

4.1 Set-up for milling on CNC machine

The figures, Figure 39 and Figure 40 show the experimental set-up consisting of three (3) accelerometers, a dynamometer, an aluminum (Al alloy 6061) block workpiece placed on the dynamometer and a milling cutting tool held by the CNC machine's tool holder. On the X-axis, 2 (two) and Y-axis, 1 (one) accelerometers are mounted to the workpiece. The accelerometers used had the sensitivity of 1.085 $\mathrm{mV/m/s^2}$, 1.050 $\mathrm{mV/m/s^2}$ and 1.062 $\mathrm{mV/m/s^2}$ respectively. The milling cutter used was KENAN METAL 1-inch diameter MS2126 tool with two flutes and the collet chuck used was Hainer Tool TD2002/BT30ER32-3.00 inch. The dynamometer used was Kistler Type 9257B.

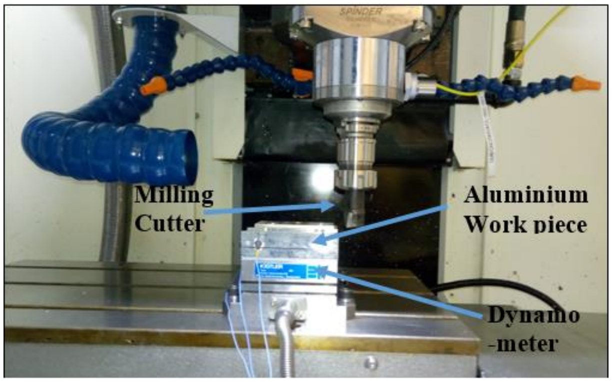

Figure 39. Experimental Set-up on CNC Machine

CUTPRO® Simulation software installed on a Sony Vaio laptop and National Instruments digital to analog converter (DAC) were used for data gathering, recording and analysis.

Figure 40. Accelerometer on work piece

The workpiece was clamped with bolts on the dynamometer and the dynamometer was clamped to the work area of the CNC machine. National Instruments (NI) digital to analog converter (DAC) was connected to the dynamometer and accelerometers to convert the analog voltage to a digital signal that got recorded by the CUTPRO® Simulation software. Modal analysis of the workpiece was conducted to obtain modal parameters associated with the three DOFs measured using the accelerometers and force hammer.

Figure 41, shows the setup used for modal analysis. The tools used for the test were a force hammer, 3 (three) accelerometers, National Instrument (NI) digital to analog converter (DAC) and the CUTPRO® Simulation software. The accelerometers used had sensitivity of 1.085 $\mathrm{mV/m/s^2}$, 1.050 $\mathrm{mV/m/s^2}$ and 1.062 $\mathrm{mV/m/s^2}$ respectively. The sensitivity of the force hammer as provided by the maker Kistler 9722A500 force hammer was 10.51 mV/lbf with a measuring range of 100lbf or 500N.

Impulse hammer tests were performed to measure the direct and cross FRFs. The natural frequencies, mode shapes, and damping ratios of the three dominant modes were extracted from measured FRFs. As a result, a 3-DOF model in modal space was constructed to describe the dynamics of the workpiece. The measured mode shapes matrix, $[\phi] \in \mathbb{R}^{3x3}$, natural frequencies, ω_n and damping ratios, ζ_n used to create the state space matrices are as

$$[A] = \begin{bmatrix} 0_{3x3} & I_{3x3} \\ [-{\omega_n}^2] & [-2\zeta_n \omega_n] \end{bmatrix}; [B] = \begin{bmatrix} 0_{3x3} \\ [\phi]^T \end{bmatrix}; [C] = \begin{bmatrix} I_{3x3} & 0_{3x3} \\ 0_{3x3} & 0_{3x3} \end{bmatrix} \text{ and } D = 0. \tag{78}$$

Here, these matrices are the state matrix, input matrix, output matrix and feed through matrix respectively. The diagonal square matrix, $[{\omega_n}^2]$ of the natural frequencies is as

$$[-{\omega_n}^2] = \begin{bmatrix} -{\omega_1}^2 & 0 & 0 \\ 0 & -{\omega_2}^2 & 0 \\ 0 & 0 & -{\omega_3}^2 \end{bmatrix}. \tag{79}$$

Similarly, $[-2\zeta_n \omega_n]$ matrix is as

$$[-2\zeta_n \omega_n] = \begin{bmatrix} -2\zeta_1 \omega_1 & 0 & 0 \\ 0 & -2\zeta_2 \omega_2 & 0 \\ 0 & 0 & -2\zeta_3 \omega_3 \end{bmatrix}. \tag{80}$$

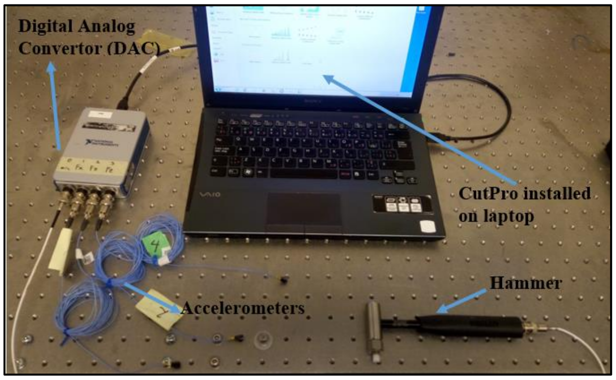

Figure 41. Set-up for Modal Analysis of work piece

4.2 Experimental Results

The experiments carried out on the CNC machine were done in two (2) stages. The 1st stage was to verify the working of the algorithm for the milling operation and it was followed by the 2nd stage to verify the repeatability under various cutting conditions.

Table 4 shows the conditions under which the measurements of vibration responses was carried out during the first stage of the experiments.

Parameter	Values
Spindle Speed	2000 rpm (revolution per minute)
Feed Rate	0.15 mm/tooth
Depth of cut	2.0 mm

<table>
<tr><td>Radial Immersion</td><td>Full immersion</td></tr>
<tr><td>Sampling Frequency</td><td>10240 hertz</td></tr>
<tr><td>Time duration of data sample</td><td>10.990 to 15.01 seconds</td></tr>
<tr><td>Total iteration number</td><td>41166</td></tr>
<tr><td colspan="2">Modal Parameters</td></tr>
<tr><td colspan="2">

The mode shapes, $[\phi] \in \mathbb{R}^{3x3}$, and the natural frequencies, $[\omega_n] \in \mathbb{R}^{1x3}$, of the 3 (three) dominant modes are as

$$[\phi] = \begin{bmatrix} 0.085 & 0.454 & 0.586 \\ 0.049 & 0.467 & -0.505 \\ -0.103 & 0.010 & -0.346 \end{bmatrix}, \tag{81}$$

$$[\omega_n] = 2\pi * [1417.828 \quad 1807.507 \quad 2481.560]\,. \tag{82}$$

Similarly, the matrix for damping ratio, $[\zeta_n] \in \mathbb{R}^{1x3}$ for the modes are as

$$[\zeta_n] = [0.016 \quad 0.044 \quad 0.026]\,. \tag{83}$$

</td></tr>
<tr><td colspan="2">Co-variance and State Initialization</td></tr>
<tr><td colspan="2">

$$[Q] = (10^{-3})I_{6x6}\ , \tag{84}$$

$$[R] = (10^{-10})I_{9x9}\ , \tag{85}$$

$$[S] = (10^{8})I_{3x3}\ . \tag{86}$$

The values for Q and R are chosen based on accuracy of the sensors and order of magnitude of the state vector. The diagonal values of, S, were taken from the L-curve plotted on Figure 46. A large value of 1.0E2, was chosen for initialization for error covariance, $[P_{0|-1}] \in \mathbb{R}^{9x9}$ and a low value was chosen for initialization of the states, $[\overline{X}^{a}_{0|-1}] \in \mathbb{R}^{9}$ as

$$[P_{0|-1}] \quad = (10^{2})I_{9x9}\ , \tag{87}$$

$$[\overline{X}^{a}_{0|-1}] = [0_{1x9}]^{T}. \tag{88}$$

</td></tr>
</table>

Table 4. Experiment with modal, cutting etc. parameter conducted during 1st stage on CNC milling machine

In the 2nd stage, experiments were carried out to verify and analyze the repeatability of cutting force reconstruction results in both the X and Y-axes. Table 5 shows the conditions under which the measurements of vibration responses were carried out during the experiments.

Modal Parameters

The mode shapes, $[\phi] \in \mathbb{R}^{3x3}$, and the natural frequencies, $[\omega_n] \in \mathbb{R}^{1x3}$, of the 3 (three) dominant modes are as

$$[\phi] = \begin{bmatrix} 0.059 & 0.396 & -0.524 \\ 0.080 & 0.377 & 0.535 \\ -0.012 & 0.009 & -0.320 \end{bmatrix}, \quad (89)$$

$$[\omega_n] = 2\pi * [598.865 \quad 1787.792 \quad 2466.208]. \quad (90)$$

Similarly, the matrix for damping ratios, $[\zeta_n] \in \mathbb{R}^{1x3}$ for the modes are as

$$[\zeta_n] = [0.019 \quad 0.035 \quad 0.021]. \quad (91)$$

The subscript, n, are 1, 2 and 3 representing the values for the 1st, 2nd and 3rd modes.

Co-variance and State Initialization

The values of Q and R, for Stage 2 were kept same as the Stage 1 values

$$[Q] = (10^{-3})I_{6x6}, \quad (92)$$

$$[R] = (10^{-10})I_{9x9}. \quad (93)$$

The diagonal values of S, for reconstruction of forces on X-axis is 1.0E6 as

$$[S] = (10^{6})I_{3x3}. \quad (94)$$

The diagonal values of S, for reconstruction of forces on Y-axis is 1.0E7 as

$$[S] = (10^{7})I_{3x3}. \quad (95)$$

$$[P_{0|-1}] = (10^{2})I_{9x9} \quad (96)$$

is set similar to Stage 1, a large value of 1.0E2 is set for error covariance, $[P_{0|-1}] \in \mathbb{R}^{9x9}$,and a low value is set for the states, $[\overline{X}^{a}_{0|-1}] \in \mathbb{R}^{9}$ for initialization as

$$[\overline{X}^{a}_{0|-1}] = [0_{1x9}]^{T}. \quad (97)$$

Condition #1: Forces Measured on X-axis (Full Immersion)

Parameter	Values
Spindle Speed	2000 rpm (revolution per minute)
Feed Rate	0.15 mm/tooth
Depth of cut	1.0 mm
Sampling Frequency	10240 hertz

Condition #2: Forces Measured on X-axis (Half Immersion)

Spindle Speed	2000 rpm (revolution per minute)
Feed Rate	0.15 mm/tooth

Depth of cut	1.0 mm
Sampling Frequency	10240 hertz
Condition #3: Forces Measured on X-axis (Changing Force Pattern)	
Spindle Speed	2000 rpm (revolution per minute)
Feed Rate	0.15 mm/tooth
Depth of cut	1.0 mm
Sampling Frequency	10240 hertz
Condition #4: Forces Measured on Y-axis (Full Immersion)	
Spindle Speed	2000 rpm (revolution per minute)
Feed Rate	0.15 mm/tooth
Depth of cut	1.0 mm
Sampling Frequency	10240 hertz

Table 5. List of experiments with modal, cutting etc. parameter conducted during 2nd stage on CNC milling machine

The equations (44) - (50) on Chapter 2, are used to regressively reconstruct the cutting forces with the augmented matrices, initial time updates and vibration response data. Cutting force $[F_{X(k|k)}] \in \mathbb{R}^9$ for each iteration was computed as

$$[F_{X(k|k)}] = [0_{1x6} \quad I_{1x1} \quad 0_{1x2}][\overline{X}^{a}(k/k)] + [0_{1x7} \quad I_{1x1} \quad 0_{1x1}][\overline{X}^{a}(k/k)]. \quad (98)$$

Here, k|k represents the estimate for the k th, iteration within the algorithm.

The cutting forces measured from the dynamometer have two (2) parts which are the static and dynamic. Table 6 shows the characteristics of the measuring devices and the force components measured.

Measurement Tool	Measurement	Component
Accelerometer	Acceleration of Vibration Response	Accelerometers measure only the vibration responses from the dynamic component of the force and the displacement part for static force part is not recorded by the device
Dynamometer	Cutting Forces in X- and/or Y-axis	Dynamometer measures both the static and the dynamic component of the force [Toh, 2004]

Table 6. Static & Dynamic component measurement by Accelerometer & Dynamometer

The spectrum analysis of the force signal [Ahna, Jeong, Yoob, 2005] measured from the dynamometer was done to compare the static and dynamic components of the force. Figure 42 shows the spectrum of the force measured by the dynamometer and the beginning of the spectrum clearly shows a static component.

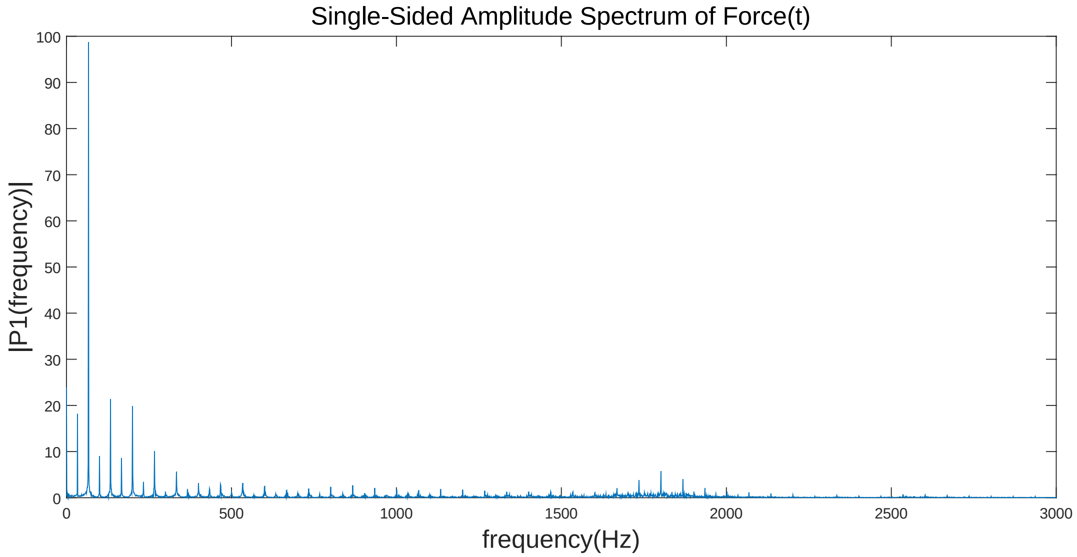

Figure 42. Frequency spectrum of force recorded from Dynamometer

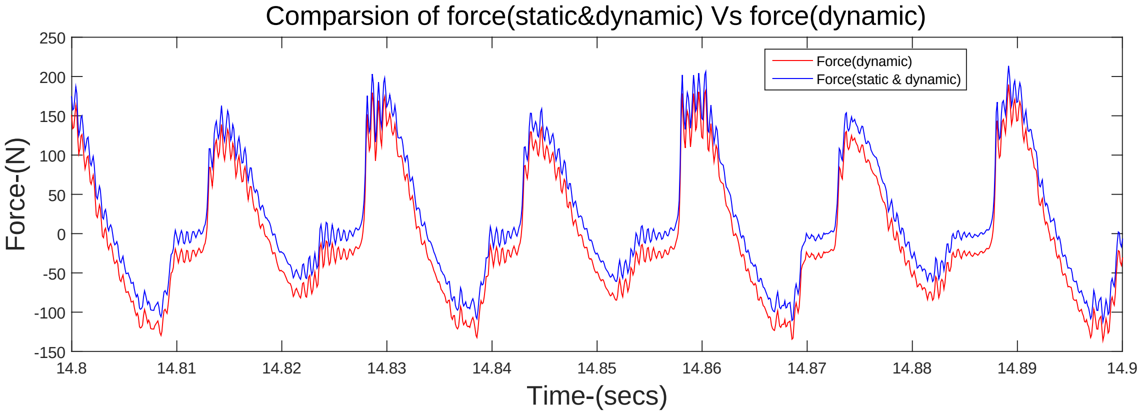

Figure 43. Comparison of forces, dynamic component (blue) versus dynamometer measurement (red) of force

Figure 43, shows the cutting force measured by dynamometer as compared to only the dynamic component of the force. Figure 44, shows the reconstructed force using the augmented Kalman method with the parameters shown on Table 4.

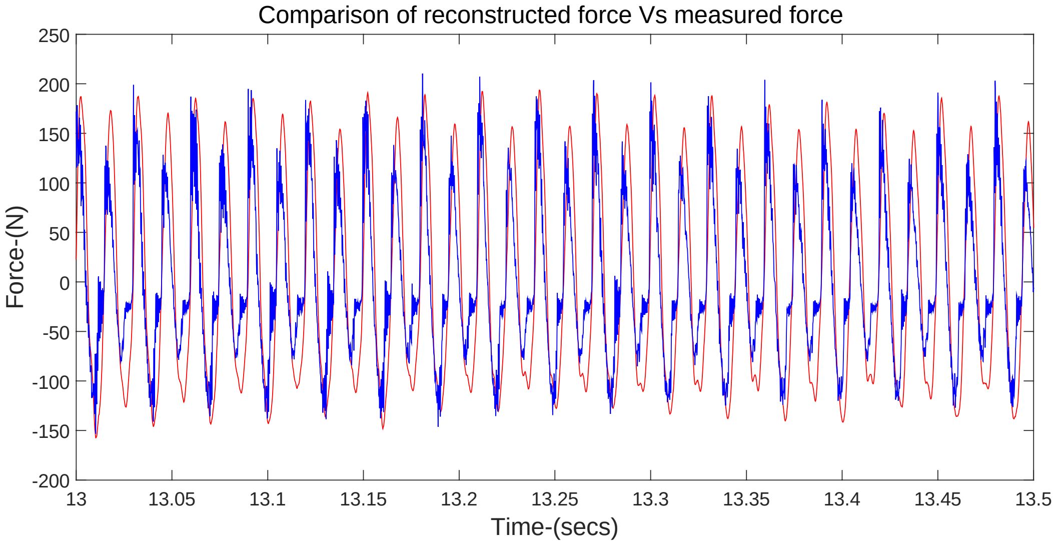

Figure 44. Actual (blue) versus reconstructed (red) force using augmented Kalman filter on CNC milling m/c for 1st stage. Values used are Q, R and S of 1.0E-3, 1.0E-10 and 1.0E8, and error covariance P of 1.0E2

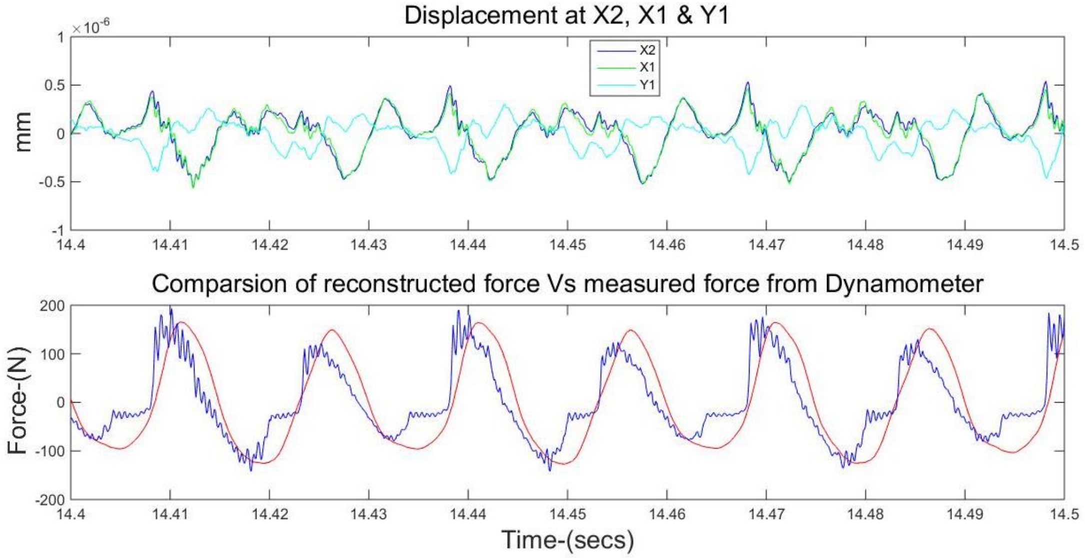

Figure 45. Graph (1st stage) for measured vibration responses (displacement) and comparison of forces – dynamometer (blue) measurement and reconstructed force (red)

Figure 45, shows the comparison graph of the displacement measurements and forces.

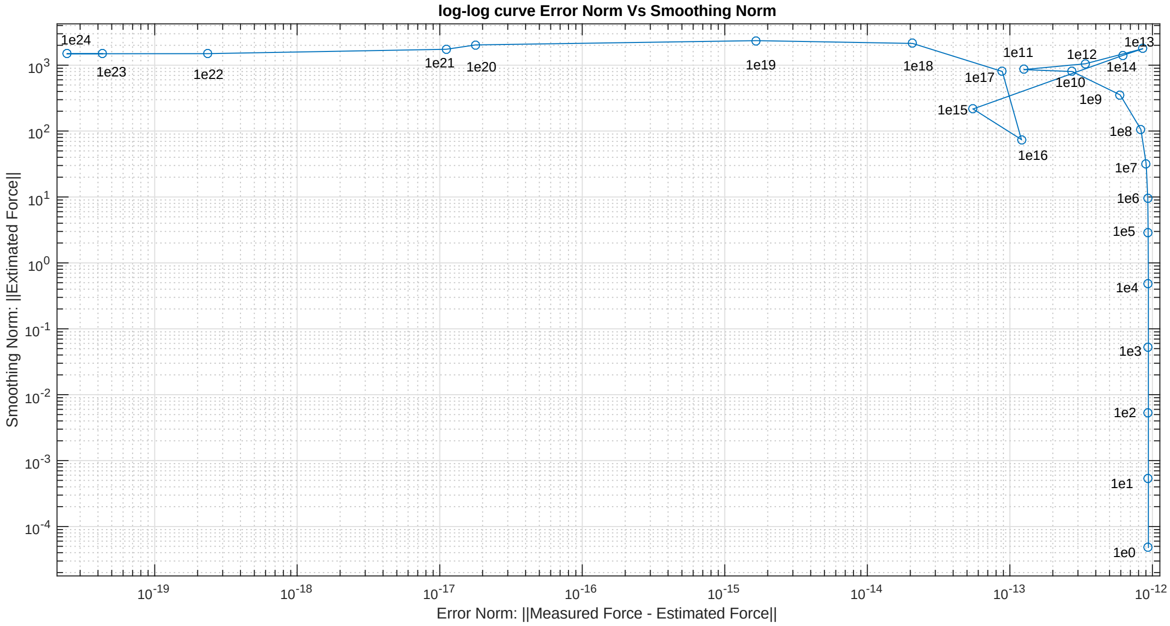

Figure 46. Graph of L-curve for 1st stage. The regularization factor does not converge on the smoothing norm and reconstruction constantly increases in magnitude. Best results obtained at S = 1.0E8.

The regularization factor for creating the co-variance matrix was 1.0E8. Figure 46 shows the L-Curve. In this case it was observed that a regularization, (E, Reynders, DeRoeck, Degrande, & G.Lombaert, 2012), factor of 1.0E8 on the L-Curve gave the best results of reconstruction. The regularization factor, on the smoothing norm of the L-Curve, does not converge like it did for the collocated measurement case of the shaker cantilever beam experiment and this is because the placement of all the accelerometers on the workpiece are non-collocated. Due to non-availability of collocated measurements an optimal regularization factor does not exist. This phenomenon is also observed by other researchers (E, Reynders, DeRoeck, Degrande, & G.Lombaert, 2012).

During the 2nd stage of the experiments, 4 types of scenarios were conducted on the milling machine. The test set-up, tools and workpiece for this stage were all kept the same as the previous stage to maintain consistency. These tests were conducted to check for the repeatability of cutting force reconstruction by the augmented Kalman filter method. Table 5 provides the details on the parameters under which experiments were conducted for this stage.

4.2.1 Condition #1: X-axis (Full Immersion)

The cutting forces were reconstructed from the displacements measured at the points X2, X1 and Y1 on the X and Y-axes of the CNC machine. The corresponding displacements and actual forces measured were also analyzed for getting better understanding of the pattern of the reconstructed force. Figure 47, shows the graph of the reconstructed force for this condition.

The graph shows that the measurements taken for displacement at the two locations on the X-axis, X2 and X1, are close in phase and magnitude when compared to the displacement measured on the Y-axis at Y1.

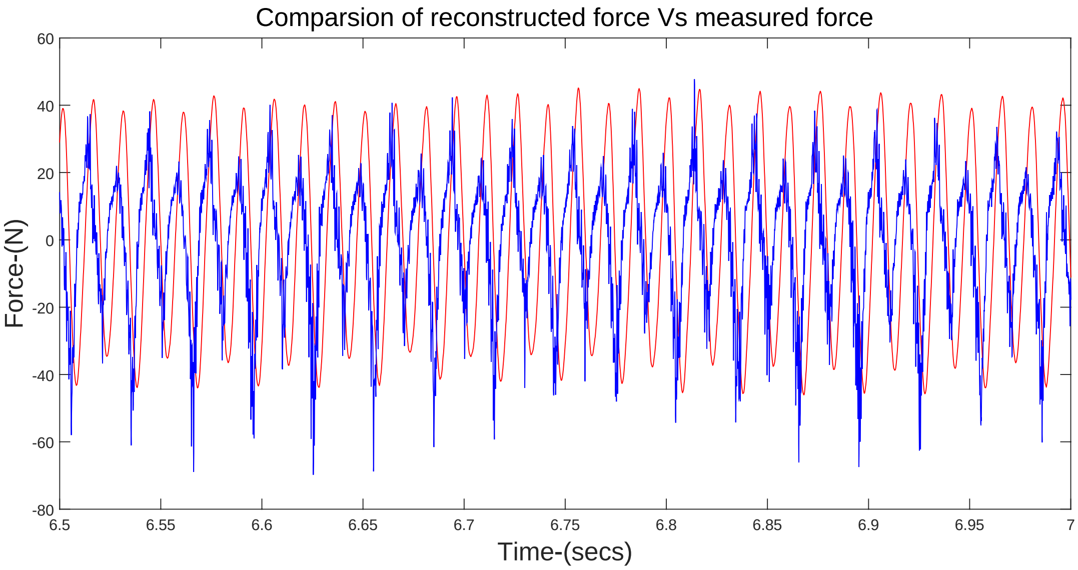

Figure 47. Actual (blue) versus reconstructed (red) force using augmented Kalman filter on CNC milling m/c for 2nd stage(condition#1). Values used are Q, R and S of 1.0E-3, 1.0E-10 and 1.0E6, and error covariance P of 1.0E2

On the other hand, the force measurement from the dynamometer had a phase which was different from the phase of the displacements on X and Y-axis. Figure 48 shows the comparison of the displacements measured and also the forces, measured and reconstructed, for the purpose of analyzing the trend of the reconstruction.

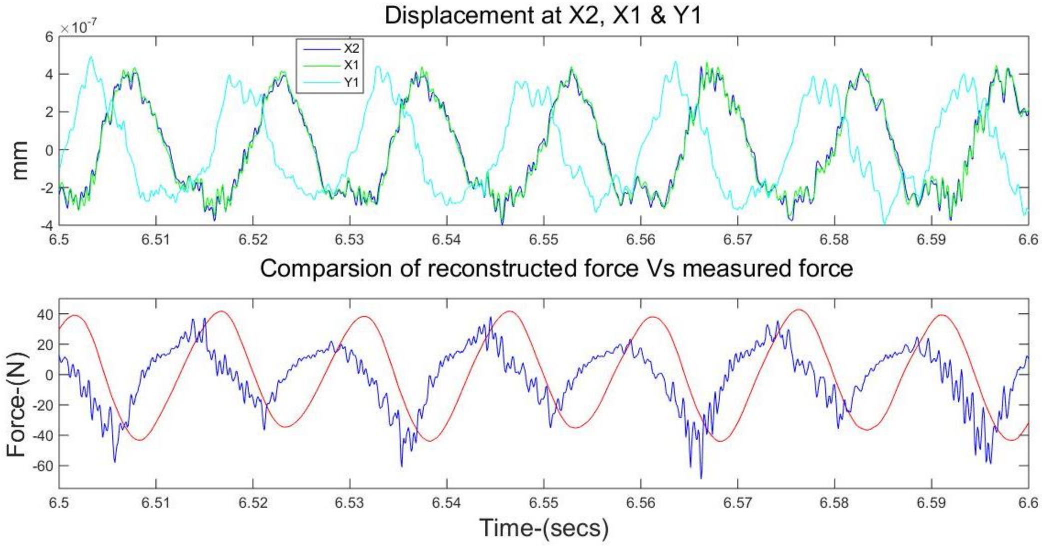

Figure 48. Graph (2^{nd} stage-condition#1) for measured vibration responses (displacement) and comparison of forces - dynamometer (blue) measurement and reconstructed force (red)

4.2.2 Condition #2: X-axis (Half Immersion)

The half immersion, up milling, experiment was done to study the performance of the augmented Kalman filter method when the cutting forces are highly interrupted and contain a higher frequency bandwidth. Figure 49 shows the graphs of the results from the method and compares the reconstructed force with the force measured using the dynamometer.

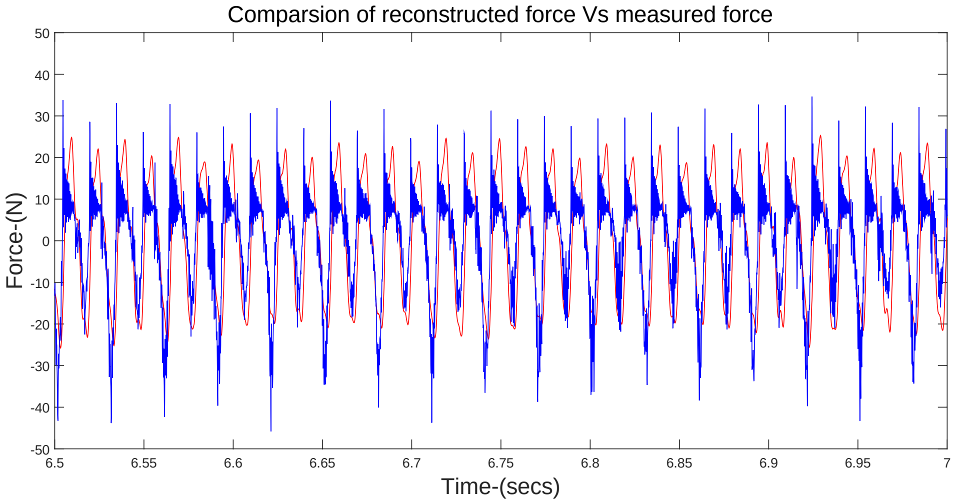

Figure 49. Actual (blue) versus reconstructed (red) force using augmented Kalman filter on CNC milling m/c for 2nd stage (condition#2). Values used are Q, R and S of 1.0E-3, 1.0E-10 and 1.0E6, and error covariance P of 1.0E2

In this case the graphs show that the flutes of the cutter when not in contact with the workpiece the force recorded by the dynamometer was close to zero.

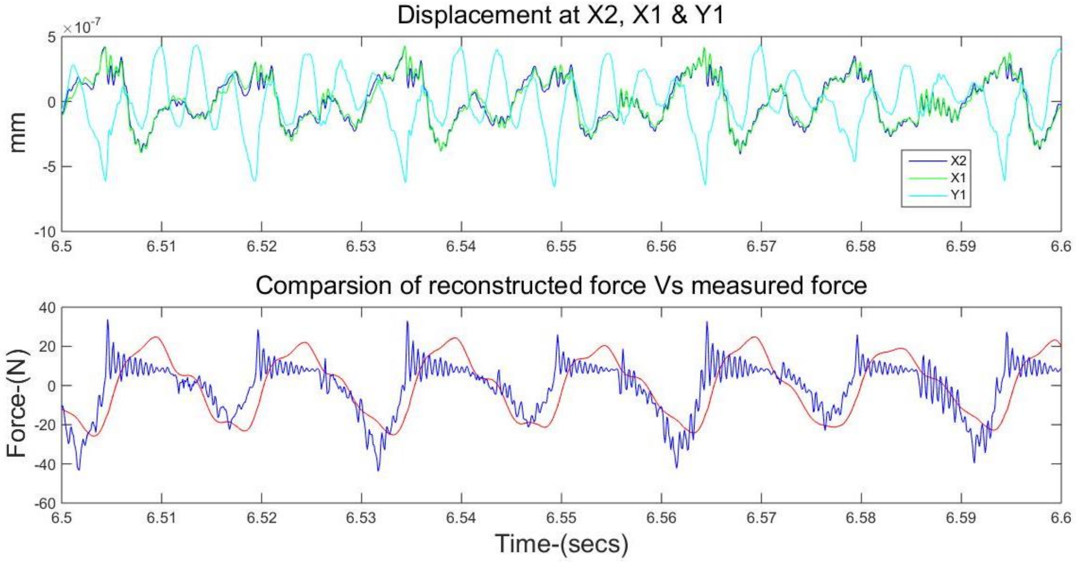

Figure 50. Graph (2nd stage-condition#2) for measured vibration responses (displacement) and comparison of forces - dynamometer (blue) measurement and reconstructed force (red)

Figure 50 show that the phase of the displacement measurements measured on the X-axis at X2 and X1 matched closely to phase of the force. Vibration responses were observed while the flutes were not in contact with the workpiece. The vibration response measurements at Y1 on the Y-axis was of a different phase and amplitude when compared to measurements on the X-axis.

4.2.3 Condition #3: X-axis (Full Immersion - Changing Force Pattern)

The full immersion milling experiment was done on an uneven surface of the workpiece on the cutting path of the milling cutter as shown on Figure 51.

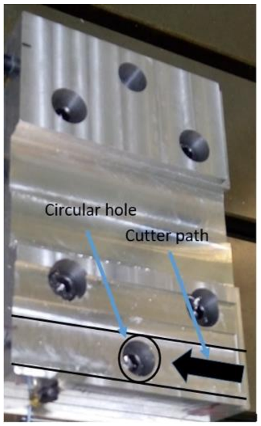

Figure 51. Circular hole on the workpiece was used as uneven patch on the cutting tool's path of the milling cutter

A patch of circular hole on the workpiece was used as the uneven surface. This was done to generate uneven cutting forces. The figures, Figure 52 and Figure 53, show the comparison of graphs for forces and displacements. Figure 52 specifically shows the force reconstruction on an even patch during the time duration from 6.7th to 7.3rd second and an uneven patch of surface from 6.4th to 6.7th second. The vibrations and reconstruction pattern both are similar to Condition#1 for the even surface but these differ for the time duration between 6.4th to 6.7th second on the uneven surface.

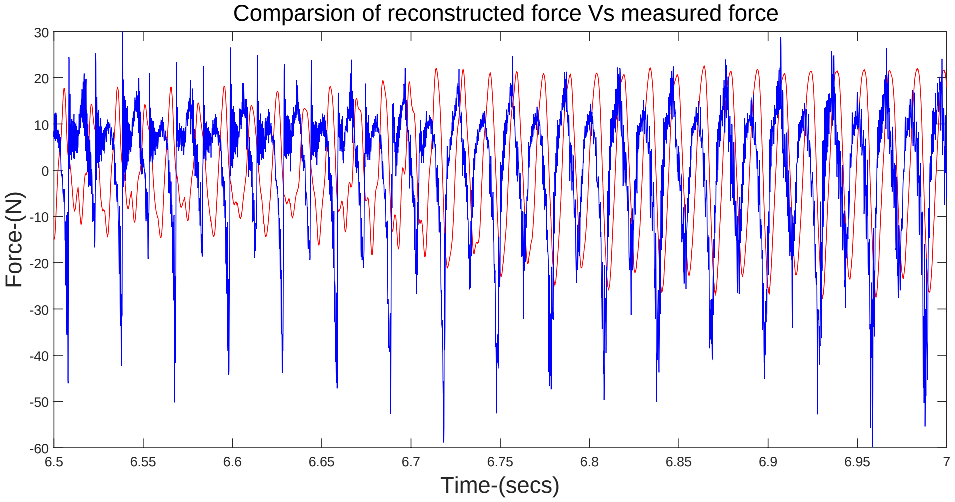

Figure 52. Actual (blue) versus reconstructed (red) force using augmented Kalman filter on CNC milling m/c for 2nd stage (condition#3). Values used are Q, R and S of 1.0E-3, 1.0E-10 and 1.0E6, and error covariance P of 1.0E2

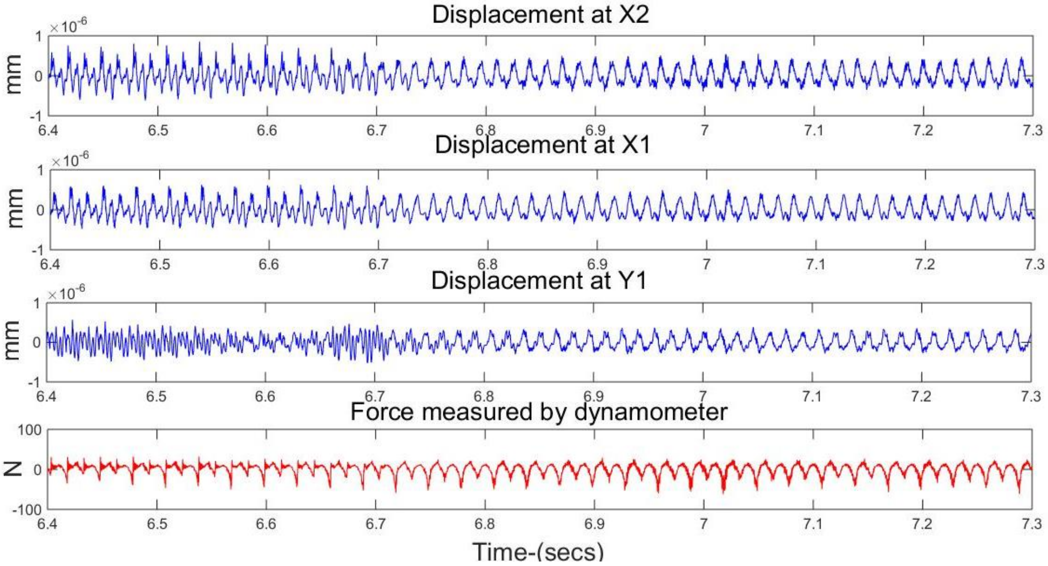

Figure 53. Graph (2nd stage-condition#3) for measured vibration responses (displacement) and dynamometer measurement for even and uneven (between 6.4 ~ 6.7 secs) patches

Figure 54 shows varying pattern of vibrations recorded by the accelerometers on the uneven surface during the time duration from 6.4th to 6.7th second. The force in the augmented state space model for augmented Kalman filter is assumed as a constant stochastic, it cannot react to fast changes in the system so the reconstruction did not match with the data recorded by the dynamometer.

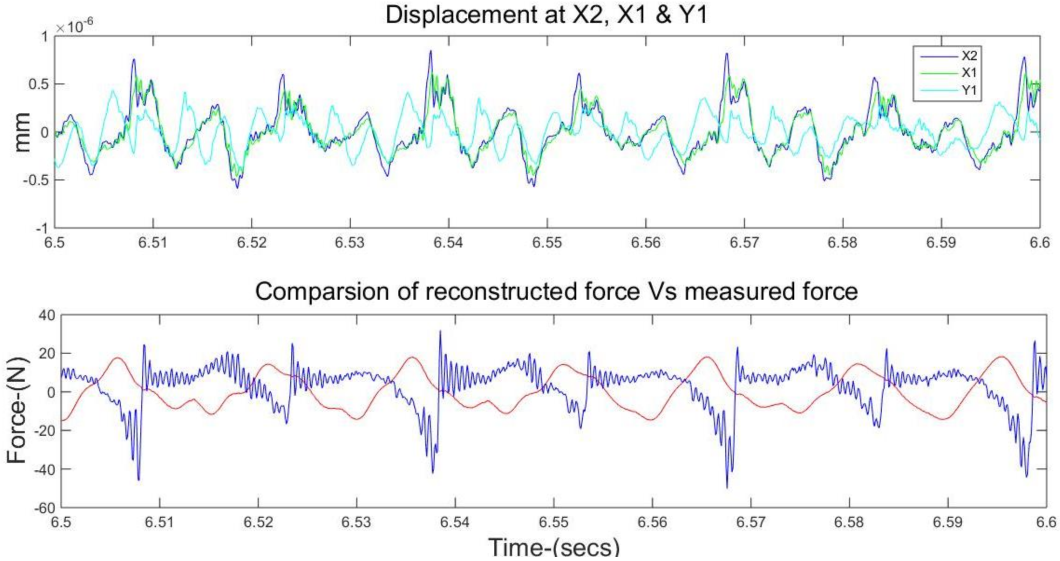

Figure 54. Graph (2^nd^ stage-condition#3) for measured vibration responses (displacement) and comparison of forces - dynamometer (blue) measurement and reconstructed force (red)

4.2.4 Condition #4: Y-axis (Full Immersion)

The full immersion milling experiment was executed with the forces measured by the dynamometer on Y-axis of the CNC machine. Figure 55 show the comparison graphs of the forces. Figure 56, shows the comparison of all the three measured displacements simultaneously and reconstructed force with dynamometer measurement. The reconstructed force from the vibration measurements shows the trend of reconstruction to the vibrations measured in the X-axis direction.

4.3 Observations on the analysis of experimental data

On our experiments, in all of the cases, the force reconstruction was done by non-collocated measurements. On the workpiece, the number of sensors were restricted to three (3) placed on the other side of the starting point of the milling cutter's cutting path. Due to use of non-collocated sensors there was a time delay for the vibration signals to reach the sensors from the location of the origin of the vibrations.

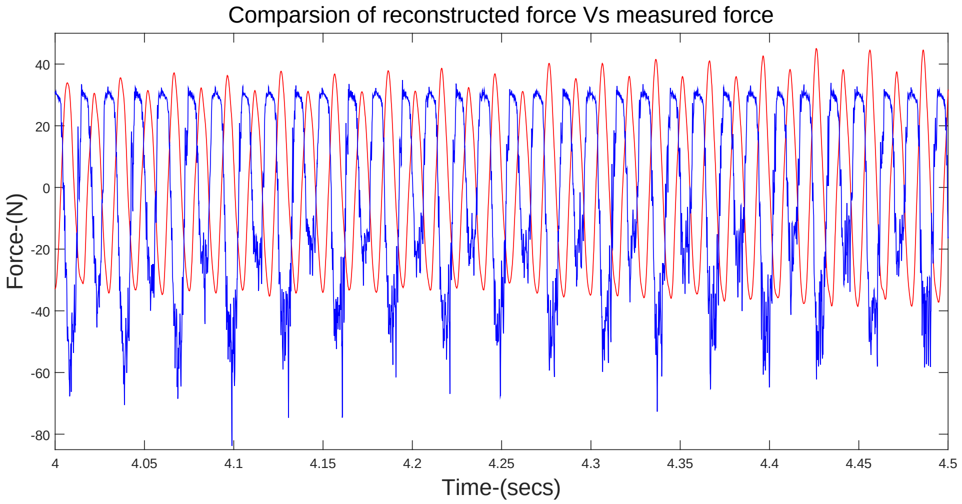

Figure 55. Actual (blue) versus reconstructed (red) force using augmented Kalman filter on CNC milling m/c for 2nd stage (condition#4). Values used are Q, R and S of 1.0E-3, 1.0E-10 and 1.0E7, and error covariance P of 1.0E2

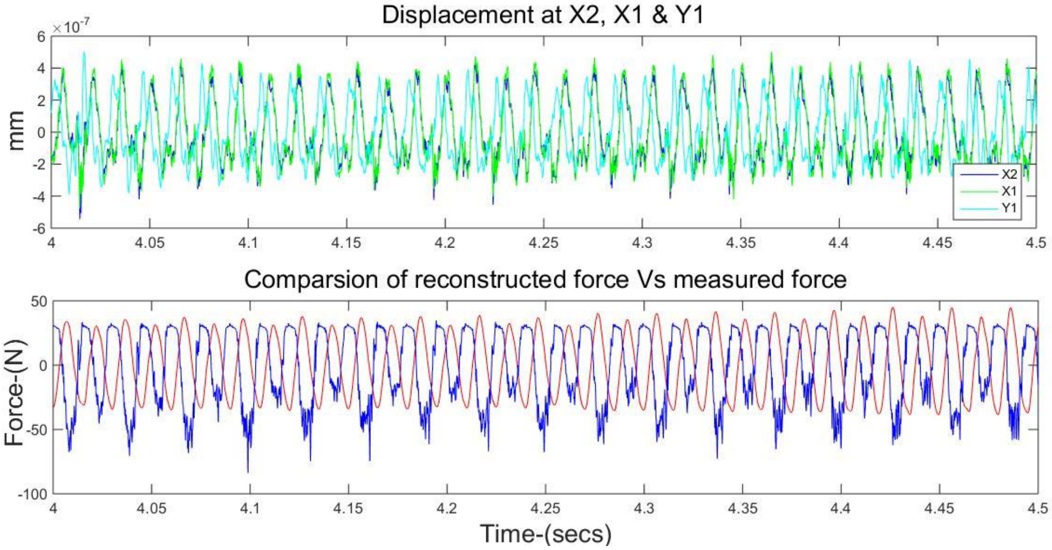

Figure 56. Graph (2nd stage-condition#4) for measured vibration responses (displacement) and comparison of forces - dynamometer (blue) measurement and reconstructed force (red)

This time delay caused slightly lesser quality of the reconstruction and this phenomenon has been observed by other researchers [E, Reynders, DeRoeck, Degrande, G.Lombaert, 2012].

As the sensors were non-collocated, the estimate of regularization from L-curve does not work and in such cases, there is need for a reference force to determine the regularization factor. The force in augmented Kalman filter is assumed constant stochastic, it cannot react to fast changes in the system. As a result, fast changes in the force cannot be predicted by this algorithm.

The Kalman filtering works best on standard system without time delay [Xiao Lua, 2004] and the inverse problem applied here for force reconstruction causes ill-conditioning at resonance [E, Reynders, DeRoeck, Degrande, G.Lombaert, 2012] for which the regularization factor was applied. The time delay of the signals reduced the quality of the reconstruction but the effect of ill-conditioning on the reconstruction was reduced by regularization factor, verified on the L-curve, in any particular direction. All reconstruction were successfully done with a single value of regularization factor of 1.0E6 for X-axis and 1.0E7 for Y-axis respectively.

Chapter 5

Conclusion and Future Work

While the problem of identifying cutting forces in machining has been given wide attention yet getting inexpensive tools to identify forces in an efficient manner is still an on-going research area. In order to conclude the thesis, this chapter highlights the key areas worked on and illustrated as

- Verification of suitability of application of regressive estimator methods like Kalman filter recursive least square, deconvolution method and augmented Kalman filter for inverse reconstruction of forces.
- Experimentally verify the applicability of real time regressive estimator, augmented Kalman filter, for cutting force estimation under different cutting conditions.

The underlying problem, in machining, that is encountered in the industry is to identify the cutting forces and undertake preventive maintenance of the machine while also solving the issue of machining inaccuracies due to vibrations from cutting forces. This thesis identifies the advantages and disadvantages of the techniques of force reconstruction and attempts to identify a cost-effective method for identification of cutting forces in real time for the milling process.

Although the deconvolution method can reconstruct the forces with vibration measurements done for measurement points near and far from the location of the excitation force (cutting force) but as the reconstruction of the forces, at any particular measurement location, is done using the vibration measurement from that particular location of measurement so it is more suited for single input single output (SISO) scenarios. In our case, milling operation, is a multi-input multi-out (MIMO) scenario. Moreover, the various deconvolution methods for force reconstruction like Greens function [E, A, P, 2003], wave reconstruction using Love’s theory and two dimensional Pochhammer frequency equation [Wu, Tsa, Tseng, 1998] are non-real-time force reconstruction techniques and our goal here was to research on online force reconstruction techniques. In this thesis Greens function was used for implementation of force reconstruction.

The thesis underscores the effectiveness of using the augmented Kalman filter method and also indicates on the scenarios where this method is not completely suitable for accurately estimating the forces.

The augmented Kalman filter method applied here for cutting force reconstruction was found to have some limitations. This algorithm, using the discrete time state measurements, does not compute the global (whole time span) time and measurement updates but only does the local (discrete time instant) computation of these updates. Thus, although, the augmented Kalman filter responds to force impact variations in cases of sudden changes on the cutting surface, as cited in section 4.6.24.64.2.3, but noise which can be acoustics emanating from vibrations of the rotating milling tool and also from high-speed spindle rotations causes large variation in the measured responses on the accelerometers. This phenomenon has been observed by other researchers [Shao, Volume 125 – No.8, 2015] and this in our case, was the cause of not so accurate reconstruction on uneven surfaces.

5.1 Future Work

In order to continue this work for identifying the cutting forces in real time scenarios of machining it is required to continue further on the work done here. On the foundations of this study and the findings from the experiments conducted on the CNC machine further future work should be done.

The experiments conducted on the workpiece were prior to measuring the characteristics of the system, the natural frequencies, mass and damping ratios etc. Thus, the data analyzed from the milling experiments underscores the fact that the system parameters are considered constant during the whole experiment. In real world, this would not be the case as the mass of the system will change due to removal of metal from the work piece during the cutting process thus resulting in the change to the natural modes of vibration.

This thesis work has put focus on identification of methods which can be applied to accurately reconstruct the cutting forces in a cost effective and efficient manner. The change in system properties during the process of milling due to removal of metal has been kept out of scope for this thesis. Thus, incorporating real time estimation techniques for estimating both the changing system parameters and simultaneously estimating the cutting forces in real time should be carried out to take ahead the work done on this thesis. An effective way for computing the regularization factor for the augmented Kalman filter method in cases of non-collocated measurements requires further study. In cases of milling having collocated sensors on the work area or workpiece has been a challenge on our experiments.

Bibliography

AhnaJinSe, JeongBongWeui, YoobSukWan. (2005). Improvement of impulse response spectrum and its application. Journal of Sound and Vibration, 1223‑1239.

An input estimation approach to on-line two dimensional inverse heat conduction problems . (2007). Numerical Heat Transfer, 345-369.

ChangC, SunC.T. (1989). Determining transverse impact force on a composite laminate by signal deconvolution. Experimental Mechanics 29 (4), 414‑419.

DoyleJ.F. (1984). Further Developments in Determining the Dynamic Contact Law. Experimental Mechanics, 265‑270.

DuJeongKim, SikDongKim. (1997). Development of a combined-type tool dynamometer with a pieze-fil accelerometer for an ultra-precision lathe. Journal of Materials Processing Technology, 360-366.

EJacquelin, ABennani, PHamelin. (2003). Force reconstruction: analysis and regularization of a deconvolution problem. Journal of Sound and Vibration, 265 (2003) 81‑107.

ELourens, ReyndersE, DeRoeckG, DegrandeG, G.Lombaert. (2012). An augmented Kalman filter for force identification in structural dynamics. Mechanical Systems and Signal Processing, 27(2012)446‑460.

Hansen, ChristianPer, O’Leary, ProstDianne. (1993). The use of the L-curve in the regularization of discrete ill-posed problems. SIAM Journal for Science and Computing, 1487-1503.

HochstenbachE.M., ReichelL., RodriguezG. (2013). Regularization parameter determination for discrete ill-posed problems.

J.KnappJ.Niemann,K.-D.WernerE.Altamann,. (1998). Measurement of shock events by means of strain gauges and accelerometers. Measurements, 87-96.

JungJuiLiu, KaoChinMa, ChungIKung, CherngDongLin. (2000). Input force estimation of a cantilever plate by using a system identification technique. Computer Methods Applied Mechanical Engineering. 190 (2000) 1309 - 1322.

KalmanE.R. (1960). A New Approach to Linear Filtering and Prediction Problems. ASME‑Journal of Basic Engineering, 82 (Series D): 35-45. Copyright © 1960 by ASME.

M.MaoX.L.Guo,Y.Zhao. (2010). Experimental study of hammer impact identification on a steel cantilever beam. Exp.Tech, 34(3)(2010)82‑85.

MaC.-K., ChangJ.-M., LinD.C. (2003). Input force estimation of beam structures by an inverse method. Journal of Sound and Vibration, 259(2), 387 ‑ 407 doi:10.1006/jsvi.2002.5334, available online at http://www.idealibrary.com.

Meirovitch, L. (1986). *Elements of Vibration Analysis.* McGrow-Hill Book Company.

Min WanMa,Jia Feng,Wei-Hong ZhangYing-Chao. (2016). Study of static and dynamic ploughing mechanisms by establishing generalized model with static milling forces. International Journal of Mechanical Sciences, 120‑131.

Najeh TounsiOthoAlain. (2000). Dynamometer Performance Modeling and Experimental Assessment. Jounal of Dynamic Systems, Mesurement, and Control, 447-485.

Pan-Chio TuanJi , Li-Wei Fong & Wen-Tang HuangChing-China. (2007). (1996) An input estimation approach to on-line two-dimensional inverse. Numerical Heat Transfer, 29:3, 345-363, DOI:10.1080/10407799608914986.

R.TranschelStirnimann, M. Blattner, B. Bill, R. Thiel, J. Stirnimann, M. BlattnerJ. (2012). Effective Dynamometer for Modeling High Dynamic Process Force Signals in Micromachining operations. 5th CIRP Conference on High Performance Cutting, (558-562).

RuneBrincker, VenturaCarlos. (2015). Introduction to operational modal analysis . John Wiley & Sons.

ShaoFu. (Volume 125 – No.8, 2015). Design of a Kalman Filter for a Cutting Force Measurement System. International Journal of Computer Applications, 13-15.

Su leyman YaldızUnsacar, Hac Saglam, Hakan IsikFaruk. (2007). Design, development and testing of a four-component milling. Mechanical Systems and Signal Processing, 1499–1511.

TohC.K. (2004). Static and dynamic cutting force analysis when high speed rough milling. Materials and Design, 41-50.

WanMin, YinWei, ZhangWei-Hong. (2016). Study of correction of cutting forces measurement with table dynamometer. 9th International Conference on Digital Enterprise Technology - DET 2016 - "Intelligent Manufacturing in the knowledge Economy Era" (119-123). Elsevier.

WuEnboa, TsaCheng-Zorn, TsengLing-Hsien. (1998). A deconvolution method for force reconstruction in rods under axial impact. Acoustical Society of America, 1418-1426.

Xiao LuaZhanga,Wei Wang, Kok-Lay TeoHuanshui. (2004). Kalman filteringfor multiple time-delay systems. Automatica, 41 (2005) 1455 – 1461.

Y.M.Mao, X.L.Guo, Y.Zhao. (2010). Experimental study of hammer impact identification on a steel cantilever beam. Exp.Tech, 82–85.

Yafei QinZhao, Yingxue Li, You Zhao, Peng WangYulong. (2017). A novel dynamometer for monitoring milling process. International Journal for Manufacturing Technology, 2555-2543.

Yen, ShinChing, EnboaWu. (1995). On the Inverse Problem of Rectangular Plates Subjected to Elastic Impact, Part I: Method Development and Numerical Verification. ASME JOURNAL OF APPLIED MECHANICS, 692-698.

ZarchanPaul, MusoffHoward. (2000). Fundamentals of Kalman Filtering - A Practical Approach. American Institute of Aeronautics and Astronautics, Inc.